UC Irvine
UC Irvine Previously Published Works

Title
Twentieth-century oceanic carbon uptake and storage in CESM1(BGC)

Permalink
https://escholarship.org/uc/item/8nx715w3

Journal
Journal of Climate, 26(18)

ISSN
0894-8755

Authors

Long, MC
Lindsay, K
Peacock, S
et al.

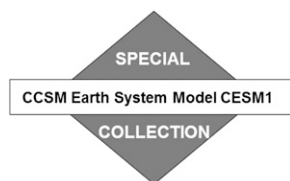**Publication Date**
2013

DOI
10.1175/JCLI-D-12-00184.1

Supplemental Material
https://escholarship.org/uc/item/8nx715w3#supplemental

Peer reviewed

SPECIAL
CCSM Earth System Model CESM1
COLLECTION

Twentieth-Century Oceanic Carbon Uptake and Storage in CESM1(BGC)*

Matthew C. Long, Keith Lindsay, and Synte Peacock

Climate and Global Dynamics Division, National Center for Atmospheric Research,[+] Boulder, Colorado

J. Keith Moore

Earth System Science, University of California, Irvine, Irvine, California

Scott C. Doney

Marine Chemistry and Geochemistry, Woods Hole Oceanographic Institution, Woods Hole, Massachusetts

ABSTRACT

Ocean carbon uptake and storage simulated by the Community Earth System Model, version 1–Biogeochemistry [CESM1(BGC)], is described and compared to observations. Fully coupled and ocean-ice configurations are examined; both capture many aspects of the spatial structure and seasonality of surface carbon fields. Nearly ubiquitous negative biases in surface alkalinity result from the prescribed carbonate dissolution profile. The modeled sea–air CO_2 fluxes match observationally based estimates over much of the ocean; significant deviations appear in the Southern Ocean. Surface ocean pCO_2 is biased high in the subantarctic and low in the sea ice zone. Formation of the water masses dominating anthropogenic CO_2 (C_{ant}) uptake in the Southern Hemisphere is weak in the model, leading to significant negative biases in C_{ant} and chlorofluorocarbon (CFC) storage at intermediate depths. Column inventories of C_{ant} appear too high, by contrast, in the North Atlantic. In spite of the positive bias, this marks an improvement over prior versions of the model, which underestimated North Atlantic uptake. The change in behavior is attributable to a new parameterization of density-driven overflows. CESM1(BGC) provides a relatively robust representation of the ocean–carbon cycle response to climate variability. Statistical metrics of modeled interannual variability in sea–air CO_2 fluxes compare reasonably well to observationally based estimates. The carbon cycle response to key modes of climate variability is basically similar in the coupled and forced ocean-ice models; however, the two differ in regional detail and in the strength of teleconnections.

1. Introduction

Over the last 200 years the ocean has absorbed 118 ± 19 Pg carbon ($1\,\text{Pg} = 10^{15}\,\text{g}$), an amount equivalent to 25%–30% of the total CO_2 emitted by fossil-fuel burning, cement production, and land-use change over this period (Sabine et al. 2004; Le Quéré et al. 2009). The ocean carbon sink has partially mitigated CO_2-induced warming by slowing the rise of atmospheric CO_2 during the anthropocene (Crutzen 2006). However, the mechanisms regulating the ocean carbon sink are sensitive to climate change; thus, uncertainty in future climate–carbon cycle interactions leads to large uncertainty in the future efficiency of the ocean carbon sink (Friedlingstein et al. 2006; Fung et al. 2005). Given strong potential for climate–carbon feedback, accurate and mechanistic representation of oceanic carbon uptake and storage is essential to robust climate prediction.

The recent Coupled Carbon Cycle Climate Model Intercomparison Project (C^4MIP) compared different models with interactive carbon cycle representations. While all the C^4MIP models agreed that climate warming will reduce the ocean carbon sink, the magnitude of the

ocean sink's sensitivity to climate varied widely among the models (Friedlingstein et al. 2006). Our ability to distinguish among disparate model estimates of climate–carbon feedbacks will rely on assessment of the relative skill of the respective ocean–carbon cycle representations.

The objective of this paper is to introduce and evaluate the ocean–carbon cycle representation in the Community Earth System Model, version 1–Biogeochemistry [CESM1 (BGC)]. Ocean carbon biogeochemistry in CESM1(BGC) is represented by the Biogeochemical Elemental Cycle (BEC) model, which has been extensively applied in the Community Climate System Model (the forerunner of CESM) framework (e.g., Moore et al. 2004; Doney et al. 2009a). CESM1 marks the first public release of the BEC model. We compare CESM1's ocean–carbon cycle in twentieth-century integrations to available observational data. Two configurations of CESM1 are considered: 1) the fully coupled Earth system model, including ocean, sea ice, land, and atmosphere models; and 2) the ocean-ice component models forced by atmospheric reanalysis data. Our analysis is aimed at identifying model biases and examining the model's twentieth-century mean state, seasonal cycle, interannual variability, and transient response. Furthermore, we explicitly test the degree to which the fully coupled model is able to represent observed atmosphere-driven variability as captured in the forced ocean-ice model. The ocean–carbon cycle response in the twenty-first century is considered in a separate paper (Long et al. 2013, manuscript submitted to *J. Climate*).

2. Numerical model

a. Model description

The Community Earth System Model is an extension of the Community Climate System Model, version 4 (CCSM4). CCSM4 is a fully coupled global climate model consisting of land, atmosphere, ocean, and sea ice components (Gent et al. 2011). CESM1(BGC) is distinguished from CCSM4 by the optional inclusion of a land-ice model, the option to use different atmospheric models, and a comprehensive global carbon cycle, including an ocean biogeochemistry module.

The physical and land surface components of the coupled model used in this paper are identical to the CCSM4 configuration discussed in Gent et al. (2011), with the exception that the depth profile of shortwave absorption in the ocean is computed using prognostic chlorophyll fields, rather than a fixed satellite-derived monthly climatology. This change has relatively little impact on the simulated climate (Lindsay et al. 2012, manuscript submitted to *J. Climate*). The atmosphere model used is the Community Atmosphere Model, version 4 (CAM4;

Neale et al. 2013) and the dynamic land-ice component is not active. CAM4 has a horizontal resolution of $1.25° \times 0.9°$ and 26 vertical layers (Neale et al. 2013). The Community Land Model, version 4 (CLM4), operates on the same horizontal grid as CAM4 (Lawrence et al. 2012). The ocean component of CESM1 is based on the Parallel Ocean Program, version 2 (POP2; Smith et al. 2010), a z-level hydrostatic primitive equation model. Danabasoglu et al. (2012) provide detailed descriptions of the various physical, numerical, and software developments included in the latest CESM ocean component and also present an analysis of model biases and physical dynamics; we make specific reference to their work throughout this paper, where the reader may find additional details relevant to the ocean biogeochemistry simulation. The CESM1 sea ice component is the Community Ice Code, version 4 (CICE4). CICE4 operates on the ocean horizontal grid; it represents a subgrid-scale ice thickness distribution and elastic–viscous–plastic rheology (Hunke and Lipscomb 2008).

In the simulations presented here, the CESM ocean component is integrated with a nominal horizontal resolution of $1° \times 1°$ and 60 vertical levels. The horizontal grid has enhanced resolution in the tropics and high latitudes; the Northern Hemisphere pole is displaced, residing over Greenland. The vertical grid spacing is 10 m in the upper 160 m and varies with depth below, increasing to 250 m by a depth of ~3500 m, then remaining constant to the model bottom at 5500 m. Physical transport terms are partitioned into resolved and unresolved components. Mesoscale eddy transport is parameterized according to Gent and McWilliams (1990; GM). The eddy-induced advection coefficient varies in space and time according to Danabasoglu and Marshall (2007). A variable coefficient provides a better representation of changes in eddy activity resulting from variable surface momentum forcing than a constant value; this is a key feature, allowing the model to more realistically capture the circulation response to changing winds, particularly in the Southern Ocean (Danabasoglu and Marshall 2007; Gent and Danabasoglu 2011; Gent 2011; Farneti and Gent 2011). Boundary layer dynamics are represented using the *K*-profile parameterization (KPP) of Large et al. (1994), with a latitudinally varying background internal wave diffusivity (Danabasoglu et al. 2012). The background diffusivities do not have depth dependence, rather abyssal tidal mixing is considered separately (Danabasoglu et al. 2012). Mixed layer restratification by submesoscale eddies is parameterized using the method of Fox-Kemper et al. (2010). Density-driven overflows through the Denmark Strait, Faroe Bank Channel, and the Ross and Weddell Seas' continental shelves are represented by an explicit parameterization (Danabasoglu et al. 2010, 2012).

Ocean carbon biogeochemistry in CESM1(BGC) is represented by the ocean Biogeochemical Elemental Cycle model embedded within the CESM ocean component. The BEC model has been described in a number of earlier papers (see Moore et al. 2004; Doney et al. 2006) and has been implemented within CESM1 with limited modification.

The surface ocean ecosystem comprises important sources and sinks for carbon. The BEC ecosystem model is built on the classical nutrient–phytoplankton–zooplankton–detritus food web model. There are three phytoplankton functional types (PFT; diatoms, "small" pico–nano phytoplankton, and diazotrophs) and one zooplankton class with PFT-specific grazing rates. Phytoplankton growth is determined as a function of temperature, multinutrient (N, P, Si, and Fe) limitation, and light availability. Carbon export and remineralization is parameterized after Armstrong et al. (2002), who specify separate remineralization length scales for mineral–ballast associated particulate organic material (POM) and purely soft tissue POM, the latter remineralizing at shallower depths. Seafloor sediment processes and storage are not represented in the model; material reaching the bottom ocean layer is remineralized in a single time step. The model solves the full nonlinear seawater carbonate system (i.e., pH, pCO_2, and bicarbonate and carbonate ion concentrations) diagnostically, as a function of prognostic dissolved inorganic carbon (DIC), alkalinity, and temperature- and salinity-dependent equilibrium coefficients (Dickson and Goyet 1994). Alkalinity is modified by the consumption and remineralization of nitrate (and ammonium), as well as biogenic calcification and dissolution of $CaCO_3$ (Najjar and Orr 1998). Biogenic calcification is modeled as proportional to a temperature-dependent fraction of small phytoplankton production; an exponential curve is prescribed to model dissolution of sinking $CaCO_3$ (Moore et al. 2002, 2004). There is no dependence of calcification–dissolution rates on saturation state. Riverine inputs into the model ocean carry no dissolved tracers and thus only contribute to the freshwater balance.

b. Model experiments

Table 1 provides a list of the numerical experiments examined in this article. Configurations denoted as "coupled" involved the CESM1(BGC) fully coupled system (i.e., atmosphere, land, ocean, and sea ice). In the ocean-ice integrations, the ocean and ice component models are forced by atmospheric observations and reanalyses, following the Coordinated Ocean–Ice Reference Experiments (CORE; Griffies et al. 2009) protocol. In these, the ocean-ice model is forced with sea–air

TABLE 1. List of numerical experiments. Obs. = observations.

Label	Configuration	BGC-CO_2*	Radiative-CO_2**	Years
CPLD1850	Coupled	284.7	Obs.	1850–2005
CPLD20C	Coupled	Obs.	Obs.	1850–2005
CORE1850	Ocean-ice	284.7	Obs.	1850–2005
CORE20C	Ocean-ice	Obs.	Obs.	1850–2007

* CO_2 used as boundary condition for BGC surface fluxes.
** CO_2 concentration used in radiative transfer calculation.

fluxes of heat, freshwater, and momentum derived using a methodology (Large and Yeager 2009) combining 6-h surface wind, temperature, specific humidity, and density from the National Centers for Environmental Prediction (NCEP) reanalysis (Kalnay et al. 1996) with satellite-based radiation, sea surface temperature, and precipitation products.

Biogeochemical fields were initialized using data-based climatologies; for instance, DIC was from the Global Ocean Data Analysis Project (GLODAP; Key et al. 2004) and nutrients were from the *World Ocean Atlas* (*WOA*; Garcia et al. 2006). Subsequently, the fully coupled model was integrated for a period of 1000 yr to allow the deep ocean to approach equilibrium; the tracer fields resulting from this spinup procedure were used to initialize a 1000-yr steady-state climate simulation (Lindsay et al. 2012, manuscript submitted to *J. Climate*), in which atmospheric CO_2 was held constant at preindustrial levels ($pCO_2^{atm} = 284.7$ ppm). In this paper, we examine two "twentieth century" simulations branched off this steady-state run after 150 years of integration.

There are multiple atmospheric CO_2 tracers in CESM1 (BGC): radiative CO_2 (rad-CO_2) and the CO_2 concentration seen as a boundary condition by the ocean and land biogeochemistry modules (BGC-CO_2) can be distinct quantities. To define a coupled control run (CPLD1850), we specify rad-CO_2 according to the instrumental record but hold BGC-CO_2 constant at the 1850 level. In the coupled transient run (CPLD20C), both CO_2 tracers (rad-CO_2 and BGC-CO_2) are identical and specified according to the observational record. While CESM1 (BGC) has the capability to model atmospheric CO_2 as a spatially explicit prognostic tracer responsive to CO_2 exchange with the ocean and terrestrial biosphere (Lindsay et al. 2012, manuscript submitted to *J. Climate*), in the experiments presented here pCO_2^{atm} has been specified as a globally uniform but annually evolving field with no seasonal cycle. The land surface model is active in the coupled integrations; however, its impact on the solution is negligible, since with prescribed pCO_2^{atm} there is no direct land–ocean communication

through the atmospheric carbon reservoir. Biogeophysical feedbacks induced by elevated pCO_2^{atm} (i.e., "greening of the land model") are very small over the twentieth century.

The initialization procedure was different for the CORE-forced runs. In these, the control simulation (CORE1850) biogeochemical fields were initialized to observed climatologies, while the physical state was taken from a CCSM4 ocean-ice hindcast run that included weak (4-yr time scale) salinity restoring to observations in the upper 50 m (Danabasoglu et al. 2012). The CORE dataset covers the period 1948–2007 (60 yr); these modern observations were used for both spinup and the twentieth-century simulation. The model was run for four repeating 60-yr forcing cycles (model years 1–240). Physical fields and dynamic tracers (temperature and salinity) were reset to their initial values (those from the previous hindcast simulation, not observations) at the beginning of each cycle. This strategy was applied to mitigate the impact of drift in the physical solution. The transient simulation (CORE20C) was branched off of CORE1850 at model year 83; thus, model years 83–240 correspond to years 1850–2007. However, it is only during the last 60 yr of the CORE-forced integrations (1948–2007; model years 181–240) that the forcing data are aligned with the time period they actually represent. Recycling the forcing data results in discontinuities where one 60-yr period ends and another begins; at these transitions, the forcing year 2007 precedes forcing year 1948 (at model year 180–181, for instance). This discontinuity shocks the system and introduces spurious flux variability (particularly in the equatorial Pacific); thus, we restrict our analysis of interannual variability of this integration to after year 1960. Further discussion of this spinup methodology and repeat forcing cycles can be found in Doney et al. (2007).

One minor difference between CPLD20C and CORE20C is that the coupled integration includes time-varying nitrogen deposition, ramping during the twentieth century (Lamarque et al. 2010), while the ocean-ice hindcast has constant nitrogen deposition; this has little impact on global-scale ocean fluxes (Krishnamurthy et al. 2007, 2009).

c. Model analysis

Oceanic DIC in the twentieth-century integrations can be divided into two components: natural and anthropogenic. Natural CO_2 (C_{nat}) is the component of ocean carbon in approximate steady-state balance with the preindustrial atmosphere. Anthropogenic CO_2 (C_{ant}) is the additional carbon absorbed by the ocean because of the atmospheric CO_2 transient. We compute fluxes and inventories of C_{ant} by subtracting simulated fields

in the control integrations (CORE1850 and CPLD1850) from those in the respective transient integrations (CORE20C and CPLD20C). The control integrations include twentieth-century climate change (see above); thus, the climate effects on C_{nat} distributions are present in both control and transient integrations and cancel in subtraction. Interannual variability in the natural carbon cycle complicates this approach somewhat. For the CORE-forced runs, physical dynamics driving carbon cycle variability are bit-for-bit identical in the control and transient simulations. Variability in each coupled model integration, however, evolves independently. To avoid introducing excessive variance into C_{ant} estimates, we compute 11-yr running means of fields in the control simulations and use these to define C_{nat}; for consistency, we use this approach for both CORE-forced and coupled integrations.

Deep-ocean drift is a separate, but related, issue involved with model analysis. Over the 156-yr integration corresponding to the twentieth century, the global ocean in CPLD1850 lost about 4 PgC, indicating the persistence of weak deep-ocean drift even after >1000 yr of spinup. Drift was not spatially homogenous but rather distributed differently in each ocean basin—similar to the model drifts in potential temperature and salinity documented by Danabasoglu et al. (2012). In the CORE-forced integration, shorter spinup resulted in larger model drift: globally the ocean gained about 12 PgC in CORE1850, distributed somewhat differently than in the coupled model, with significant accumulation of DIC in the eastern part of basins in tropical regions. The impact of model drift on estimates of the C_{ant} perturbation is relatively small since comparable drift occurs in both control and transient integrations and is therefore linearly corrected by subtraction.

To separate biases related to freshwater inventories from those associated with the carbon cycle representation, we make use of salinity-normalized quantities. These we denote with a small s (i.e., $sDIC = DIC \times \overline{S}/S$, where $\overline{S} = 35$; Sarmiento and Gruber 2006). This approach removes much of the variability in DIC and alkalinity fields associated with the concentrating (diluting) freshwater fluxes of evaporation (precipitation) or ice formation (melt; Doney et al. 2009a).

In considering biases in surface variables that affect ocean CO_2 uptake, we make use of "equilibrium DIC" (DIC_{eq}), which is the DIC concentration of seawater at equilibrium with pCO_2^{atm}. For a given value of pCO_2^{atm}, we compute DIC_{eq} from surface temperature, salinity, phosphate, silicate, and alkalinity, using published thermodynamic relationships (Dickson and Goyet 1994). To investigate the effect of biases in temperature and alkalinity on DIC_{eq}, we compute DIC_{eq} using data

from observational climatologies but replace the observed field of interest with the modeled field.

To investigate climate-driven variability in carbon cycle dynamics, we compute monthly anomalies of related fields as $Y' = Y - \overline{Y}_{\text{mon}}$, where $\overline{Y}_{\text{mon}}$ is the monthly climatology of field Y and the prime denotes the anomaly. Following Doney et al. (2009a), we construct linear Taylor series expansions of the monthly anomalies at each grid point in terms of anomalies in the driving mechanisms X':

$$Y' \approx \sum_i \frac{\partial Y}{\partial X_i} X_i' + \mathcal{O}(X_i'^2, X_i' X_j'). \quad (1)$$

Sea–air exchange of CO_2 is computed as

$$J_{\text{CO}_2} = (1 - f_{\text{ice}}) k^{\text{CO}_2} \alpha (p\text{CO}_2^{\text{sw}} - p\text{CO}_2^{\text{atm}}), \quad (2)$$

where f_{ice} is the fraction of the sea surface covered by ice, α is the temperature- and salinity-dependent CO_2 solubility (Weiss 1974), and k^{CO_2} is the gas transfer velocity, calculated as a quadratic function of wind speed as well as the temperature-dependent Schmidt number (Wanninkhof 1992). The terms $p\text{CO}_2^{\text{sw}}$ and $p\text{CO}_2^{\text{atm}}$ are the partial pressure of CO_2 in the surface ocean and atmosphere, respectively.

To examine mechanisms driving monthly anomalies of sea–air CO_2 flux [Eq. (2)], a decomposition similar to (1) can be applied:

$$J_{\text{CO}_2}' = \underbrace{(k\alpha)' \overline{\Delta p\text{CO}_2}}_{\text{I}} + \underbrace{\overline{(k\alpha)} \Delta p\text{CO}_2'}_{\text{II}} + \underbrace{[(k\alpha)' \Delta p\text{CO}_2' - \overline{(k\alpha)' \Delta p\text{CO}_2'}]}_{\text{III}}, \quad (3)$$

where the right-hand side terms represent the contribution to sea–air flux variability from variation in ice cover and the gas transfer velocity [term I; $k = (1 - f_{\text{ice}}) k^{\text{CO}_2}$, Eq. (2)], $\Delta p\text{CO}_2$ anomalies (term II), and the cross term corrected for the mean of the cross-term anomalies (term III). Our analysis of model results indicates that the cross terms contribute little to the variability in J_{CO_2}', which is consistent with the findings of Doney et al. (2009a); we therefore focus on contributions from terms I and II. The piston velocity formulation includes temperature dependence, through its dependence on the Schmidt number. Temperature-induced variability in k and α approximately cancel; therefore, term I predominately reflects fluctuations in wind speed, with an additional contribution from variability in fractional ice cover (Doney et al. 2009a).

A similar linear decomposition can be applied to monthly $p\text{CO}_2^{\text{sw}}$ anomalies:

$$p\text{CO}_2' \approx \frac{\partial p\text{CO}_2}{\partial T} T' + \frac{\partial p\text{CO}_2}{\partial S} S' + \frac{\partial p\text{CO}_2}{\partial \text{fw}} \text{fw}' + \frac{S}{\overline{S}} \frac{\partial p\text{CO}_2}{\partial \text{DIC}} s\text{DIC}' + \frac{S}{\overline{S}} \frac{\partial p\text{CO}_2}{\partial \text{Alk}} s\text{Alk}', \quad (4)$$

where the terms on the right-hand side represent, respectively, the effect of variability in sea surface temperature, salinity (solubility), concentrating–diluting freshwater effects (fw) (see Lovenduski et al. 2007), salinity-normalized DIC, and alkalinity (Alk) (Doney et al. 2009a).

Much of the variability in $p\text{CO}_2^{\text{sw}}$ is driven by changes in surface DIC, for which we use the upper ocean (0–100 m)

DIC inventory as a proxy. Monthly anomalies of the DIC inventory can be partitioned as follows:

$$\int_0^{100} \left(\frac{\partial \text{DIC}'}{\partial t} \right) dz = J_{\text{CO}_2}' + J_{\text{virtual}}' + J_{\text{bio}}' + J_{\text{phy}}', \quad (5)$$

where J_{CO_2} is the air–sea CO_2 flux, J_{virtual} is the virtual flux of DIC in the volume conserving model due to freshwater exchange, J_{bio} is the vertically integrated net biological effect on DIC (i.e., net community production), and J_{phy} is the vertically integrated net physical transport of DIC into the top 100 m due to advection and mixing (in this case, including both resolved and unresolved processes).

To characterize the mechanisms driving the response to climate variability, we compute indices characterizing three dominant modes of climate variability: El Niño–Southern Oscillation (ENSO; Trenberth 1997), the southern annular mode (SAM; Thompson and Solomon 2002), and the North Atlantic Oscillation (NAO; Hurrell 1995). We then regress the biogeochemical anomalies (Y') and anomaly components [$(\partial Y/\partial X) X_i'$] onto the climate indices (Ψ_j) at each grid point,

$$\frac{\partial Y}{\partial X_i} X_i' = \beta_{ij} \Psi_j, \quad (6)$$

using linear least squares regression to estimate β_{ij}. We take the β_{ij} to represent the effect of climate-driven variability in X_i on the anomalies Y'. So as to facilitate comparison of patterns across each of the modes, we standardize each climate index by dividing by its standard

deviation. All metrics of significance presented are relative to the 95% level. We take autocorrelation into account in computing significance by reducing degrees of freedom (DF) according to $DF = N \times (1 - r_1)/(1 + r_1)$, where N is the original sample size and r_1 is the lag-one autocorrelation (Zwiers and von Storch 1995).

In the examination of multidecadal trends in pCO_2, we use the approach of Takahashi et al. (2002) to separate trend components driven by changes in temperature from those related to increasing DIC and equilibrium effects, such as changes in alkalinity.

3. Observational datasets

Modeled surface ocean pCO_2 and sea–air fluxes are compared to those of Takahashi et al. (2009). Global-scale sea–air CO_2 fluxes are not observed directly; rather, Takahashi et al. (2009) combine observations of the sea–air pCO_2 difference (ΔpCO_2) with bulk gas exchange parameterizations driven by wind speed data (reanalyses) to estimate sea–air CO_2 fluxes (e.g., Takahashi et al. 1997, 2002, 2009). The Takahashi et al. (2009) climatology is available at a monthly resolution on a $4° \times 5°$ grid and is produced for the reference year 2000. When comparing model output to Takahashi et al. (2009), we use 11-yr averages centered on 2000. We also make use of the ΔpCO_2-based flux estimates of Park et al. (2010). Park et al. (2010) use empirical relationships to estimate ΔpCO_2 from SST fields; combined with wind speed, these data characterize interannual variability in sea–air CO_2 fluxes at a monthly resolution for the period 1990–2009 on the same grid as Takahashi et al. (2009), excluding sea ice affected regions south of 60°S, the Arctic Ocean, and coastal–marginal seas.

Model pCO_2^{sw} is output as pCO_2 in dry air ($pCO_{2,dry}^{sw}$), whereas observational pCO_2^{sw} datasets are provided as values at 100% humidity ($pCO_{2,wet}^{sw}$). To convert the modeled pCO_2^{sw} to wet values we use

$$pCO_{2,wet}^{sw} = pCO_{2,dry}^{sw} \left(\frac{P}{P - pH_2O} \right), \qquad (7)$$

where P is the ambient atmospheric pressure (atm) and pH_2O is determined as a function of sea surface temperature and salinity according to Weiss and Price [1980, their Eq. (10)].

Observationally based alkalinity, dissolved inorganic carbon, and chlorofluorocarbon distributions are taken from the GLODAP database (Key et al. 2004). The data that make up GLODAP were collected over the 1990s; thus, when comparing model output to these data, we use 11-yr averages centered on 1995—this approach is used to diminish the impact of interannual variability on

comparisons. GLODAP climatologies are available on a $1° \times 1°$ horizontal grid with 33 vertical levels, which we interpolate to the model grid. GLODAP reports constituent concentrations per mass of seawater. Since the CESM ocean component is volume conserving, we convert observation-based concentrations to per-volume units using a constant reference density, $\rho_0 = 1026 \, kg \, m^{-3}$. Anthropogenic CO_2 concentration estimates included in GLODAP are based on the ΔC^* methodology (Gruber et al. 1996). There are important known biases in the ΔC^*-derived C_{ant} estimates; they tend to be systematically too high in the upper ocean, too low in the deep ocean, and the global inventory is likely overestimated by about 7% (Matsumoto and Gruber 2005).

In addition to ΔpCO_2-derived flux estimates, we compare modeled annual-mean sea–air flux estimates to those derived from an ocean inversion employing GLODAP (Gruber et al. 2009). Inversion methods employ ocean general circulation models (OGCM) to solve for transport and mixing into the ocean interior: OGCMs are seeded with tracers at the ocean surface. Regional flux estimates are obtained by finding the linear combination of tracers from different regions that most closely match interior observations (Mikaloff Fletcher et al. 2006, 2007; Gruber et al. 2009). Ocean inversions have the distinct advantage of providing separate regionally resolved estimates for natural and anthropogenic flux components; however, since the ocean carbon data used to constrain the inversion require several years to collect, the flux estimates obtained are necessarily static in time and aliased by variability over the observational period. Furthermore, the inversion methodology is subject to errors in the data-based estimates of C_{ant} and, as currently implemented, relies on time-invariant circulation fields from OGCMs with potential biases. The C_{ant} flux estimates are not very sensitive to biases in the vertical distribution of ΔC^*-derived C_{ant}; however, the globally integrated C_{ant} fluxes scale in proportion to the C_{ant} inventory bias (Mikaloff Fletcher et al. 2006)—thus we might expect these fluxes to be biased high by about 7% (cf. Matsumoto and Gruber 2005). We make use of the same regional definitions as Gruber et al. (2009), consolidating their original 30 regions into 12 aggregate regions.

4. Results and discussion

a. Annual-mean surface properties

The overall spatial pattern of modeled ΔpCO_2 ($\Delta pCO_2 = pCO_2^{sw} - pCO_2^{atm}$) agrees reasonably well with observations (Table 2), with positive ΔpCO_2 values in the tropics and weakly negative values at midlatitudes.

TABLE 2. Comparison of global annual-mean biogeochemical fields from CESM1 (mean over 1990–2000) and observational data. The Arctic is excluded from comparisons because of a paucity of observations. See Doney et al. (2009b) for a description of the metrics presented.

Variable	Units	Mean			Bias		RMS error		Correlation	
		Obs.	CORE	CPLD	CORE	CPLD	CORE	CPLD	CORE	CPLD
SST[a]	°C	19.12	19.15	19.49	0.0	0.4	0.5	1.1	>0.99	>0.99
SSS[b]	psu	34.81	34.90	34.47	0.1	−0.3	0.3	0.6	0.95	0.88
$p\mathrm{CO}_2^c$	ppmv	358	367	367	8.6	8.7	17	19	0.80	0.77
$s\mathrm{DIC}^d$	mmol m^{-3}	2082	2068	2070	−14	−13	29	28	0.97	0.96
$s\mathrm{Alk}^e$	mmol m^{-3}	2377	2353	2352	−25	−25	33	35	0.73	0.70
RF[f]		10	10	11	0.2	0.5	0.6	0.8	0.97	0.97
C_{ant}^g	mol m^{-2}	27	21	22	−5.4	−4.5	9.3	8.9	0.86	0.87
		(101)	(85)	(89)						
CFC-11[h]	μmol m^{-2}	1.6	1.4	1.5	−0.2	−0.1	0.8	0.7	0.86	0.89
		(5.15×10^8)	(4.73×10^8)	(4.97×10^8)						

[a] Sea surface temperature observations from Hurrell et al. (2008).
[b] Sea surface salinity observations from *WOA*.
[c] Sea surface $p\mathrm{CO}_2$ observations from Takahashi et al. (2009).
[d] Sea surface dissolved inorganic carbon (salinity normalized) observations from GLODAP.
[e] Sea surface salinity-normalized alkalinity observations from GLODAP.
[f] Sea surface Revelle factor computed from GLODAP and *WOA* data.
[g] Column inventory of anthropogenic CO_2 observations from GLODAP, excluding marginal seas and Arctic Ocean. Numbers in parentheses below means are the respective global inventories (PgC) computed on the model grid.
[h] Column inventory of CFC-11 observations from GLODAP, excluding marginal seas and Arctic Ocean. Numbers in parentheses below means are the respective global inventories (mol) computed on the model grid.

Modeled $\Delta p\mathrm{CO}_2$ is larger than observed in the eastern equatorial Pacific and over much of the Southern Ocean north of about 60°S, especially in the Indian Ocean sector (Figs. 1b,c). The term $\Delta p\mathrm{CO}_2$ is under-estimated, by contrast, in the polar Southern Ocean, particularly in the coupled model (Figs. 1b,c); in this region, the model predicts $\Delta p\mathrm{CO}_2$ values of the opposite sign to those of Takahashi et al. (2009).

Both model configurations capture the overall spatial structure in annual-mean salinity-normalized surface DIC and alkalinity, evident in high-correlation coefficients relative to GLODAP (Table 2). However, modeled salinity-normalized surface DIC and alkalinity concentrations tend to be too low over much of the ocean, with global-mean biases of about −13 and −25 mmol m^{-3}, respectively (Table 2). Qualitatively, there is some similarity between the spatial distribution of positive biases in $\Delta p\mathrm{CO}_2$ and positive biases in sDIC (Fig. 1), with patches of elevated sDIC in the equatorial Pacific and Southern Ocean. The correlation between these bias fields is not significant at the 95% level, however, and other factors, such as alkalinity, contribute to variations in the sDIC–$p\mathrm{CO}_2^{sw}$ relationship. It is also important to note that $p\mathrm{CO}_2^{sw}$ computed from GLODAP surface fields is not strictly consistent with Takahashi et al. (2009) since $p\mathrm{CO}_2$ is a nonlinear function of the gridded fields. Salinity-normalized surface alkalinity is underestimated virtually everywhere in both model configurations, especially in the North Pacific (Table 2), with the exception of equatorial regions in the Pacific and Indian Oceans and in the Weddell Sea (Figs. 1h,i). Alkalinity is, in fact, biased low throughout the upper water column in both models but over estimated at depth (Moore et al. 2013). Deficiencies in the prescribed dissolution curve for sinking CaCO_3 may contribute to these biases, as the near-surface rain ratio and export magnitudes are reasonable (Moore et al. 2013).

In a closed system, DIC and alkalinity induce effects of opposing tendency (but unequal magnitude) on $p\mathrm{CO}_2^{sw}$: low biases in DIC depress $p\mathrm{CO}_2^{sw}$ values, while low alkalinity pushes $p\mathrm{CO}_2^{sw}$ higher. Thus, in regions where DIC is low, the effect of low alkalinity may result in elevated $p\mathrm{CO}_2^{sw}$. The northeastern Pacific, for instance, has both negative DIC and alkalinity biases but positive $\Delta p\mathrm{CO}_2$ bias (Fig. 1). The negative bias in surface alkalinity would result in a negative bias in DIC_{eq} of about 50–60 mmol m^{-3} over much of the ocean in the coupled model (see supplementary materials, Fig. S1).

Much of the surface ocean is not at equilibrium with respect to atmospheric CO_2, and biases in DIC_{eq} provide only a qualitative sense of surface chemistry impacts on CO_2 uptake. Low alkalinity causes the surface ocean to more quickly saturate with respect to a perturbation in atmospheric CO_2, thereby contributing to diminished CO_2 uptake in transient simulations. The Revelle factor [RF = $\mathrm{DIC}/p\mathrm{CO}_2(\partial p\mathrm{CO}_2/\partial\mathrm{DIC})$] quantifies this effect:
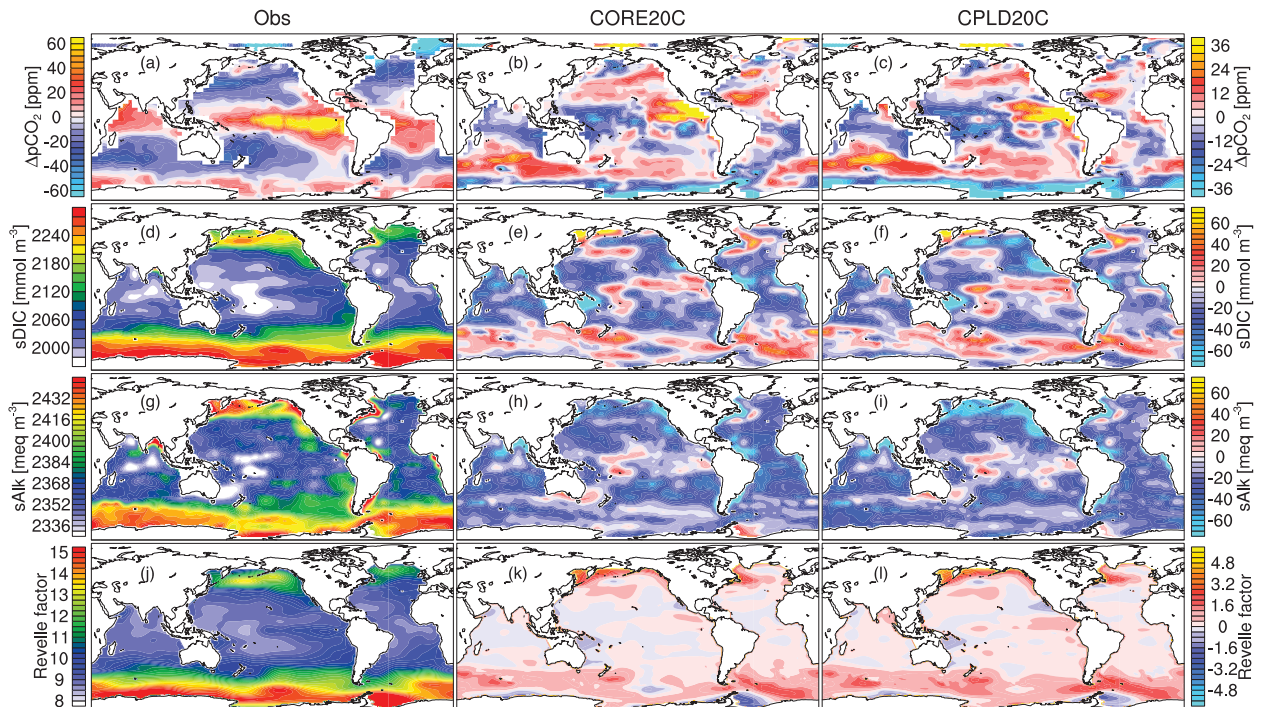
FIG. 1. (left) Observationally based climatologies of surface fields. Biases relative to observations in (center) CORE20C, and (right) CPLD20C. (a)–(c) Annual-mean sea–air pCO_2 difference (ΔpCO_2; Takahashi et al. 2009). (d)–(f) Salinity-normalized dissolved inorganic carbon, (g)–(i) salinity-normalized alkalinity, and (j)–(l) Revelle factor (Key et al. 2004). The Revelle factor was computed analytically from the thermodynamic equations.

a high RF indicates a smaller change in DIC per unit change in pCO_2; therefore, a high RF results in reduced CO_2 uptake from the anthropogenic transient. Negative biases in alkalinity contribute to a net positive bias in the model's global-mean RF (Table 2; Fig. 1). The RF is sensitive to the DIC:alkalinity ratio; thus, there is some spatial correspondence between positive biases in DIC and the RF (Fig. 1).

Temperature and salinity also affect carbonate equilibrium chemistry. Weak salinity restoring in the CORE-forced runs and the use of observationally based forcing data lead to smaller biases in sea surface temperature and salinity in this integration relative to the coupled model (Table 2). Since CO_2 solubility increases with decreasing temperature, biases in DIC_{eq} are negatively correlated with biases in SST (Fig. S1). For instance, the coupled model SST tends to be too warm in subtropical eastern boundary currents and too cold at high latitudes and in the Gulf Stream and Kuroshio regions (Danabasoglu et al. 2012). The most pronounced positive effects of SST on DIC_{eq} in the coupled model are evident in the Southern Ocean and south of Greenland, where SST are too cold (Fig. S1). These effects offset the negative influence of low alkalinity somewhat but overall the total DIC_{eq} bias is quite similar to the alkalinity effect

(Fig. S1), demonstrating that alkalinity biases dominate over those in SST.

Examination of the surface DIC and alkalinity fields requires some care since the observations reflect processes not in the models. For instance, large but localized negative biases in salinity-normalized DIC and alkalinity in the Atlantic and Indian Ocean basins reflect terrestrial carbon and weathering inputs from the Congo, Amazon, and Ganges/Brahmaputra Rivers that are not included in the model (Fig. 1).

b. Seasonality

In the stratified subtropical ocean, seasonal variability in pCO_2^{sw} is predominantly related to changes in SST: summer warming increases pCO_2^{sw}, whereas winter cooling drives decreases it (Takahashi et al. 2002). In contrast, in the subpolar ocean, winter is characterized by opposing effects of cold SSTs and entrainment of CO_2-rich deep water by vertical mixing—in summer, warming drives pCO_2^{sw} up, while biological CO_2 drawdown by phytoplankton drives it down. CESM1 captures the resulting seasonality in pCO_2^{sw} quite well over most oceanic regions (Fig. 2). Two notable exceptions are the polar Southern Ocean and the high-latitude North Atlantic (49°–80°N).
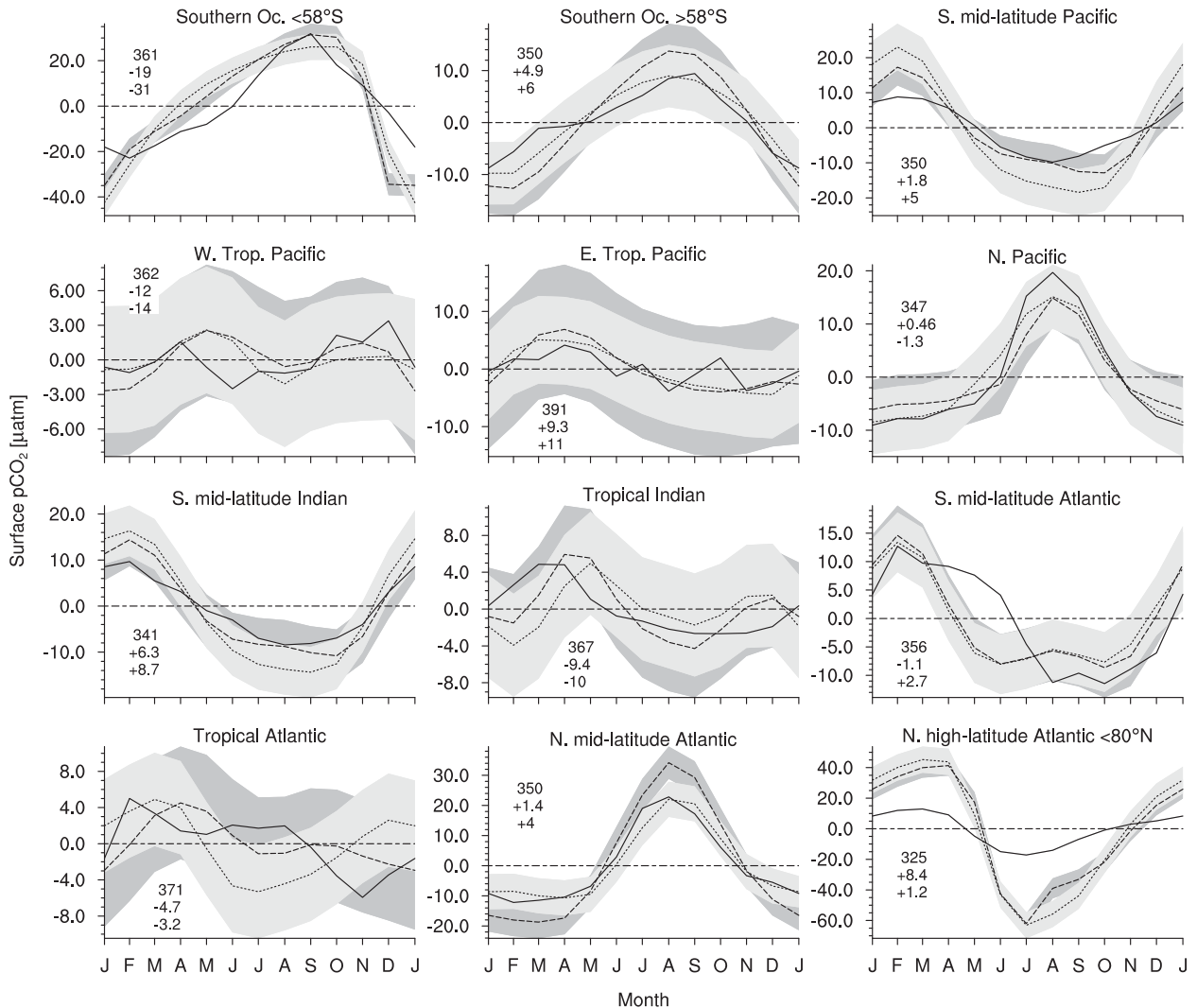
FIG. 2. Seasonal cycle of pCO_2 by region from the monthly climatology of Takahashi et al. (2009; solid), CORE20C (dashed), and CPLD20C (dotted). Model data are from years 1995–2005, bracketing reference year 2000 used in the observations. The annual mean has been subtracted from each series; in each plot, the column of numbers shows, in order from top to bottom, the annual mean (ppm) of the observations then the CORE20C and CPLD20C annual-mean biases. Shaded regions show the range of interannual variability ($\pm 1\sigma$) in CORE20C (dark gray), and CPLD20C (light gray) for the same 10-yr period. Regional definitions are the same as those in Gruber et al. (2009).

In the polar Southern Ocean, annual-mean pCO_2^{sw} is substantially lower in the model than in observations (Figs. 1, 2) and the model predicts stronger seasonality, with much lower austral summer December–February (DJF) pCO_2^{sw} values than in the Takahashi et al. (2009) climatology (Fig. 2). The cause of these biases may involve overestimation of summertime net primary productivity. Summertime mixed layer depths along the Antarctic Circumpolar Current (ACC) are too shallow in the model by 20–50 m (Danabasoglu et al. 2012; Moore et al. 2013). Thus, the seasonal drawdown of DIC occurs in a mixed layer that is much shallower than observed; light limitation of phytoplankton growth rates is therefore underestimated, leading to reduced pCO_2 in the austral summer

and a depressed annual mean. The sparsity of observations in the Southern Ocean, particularly during winter months, may also contribute. To compensate for winter data gaps, Takahashi et al. (2009) assume that pCO_2 increases linearly with time in ice-covered waters. This assumption may unrealistically inflate the annual-mean pCO_2^{sw}. Furthermore, the coarse resolution ($4° \times 5°$) of the Takahashi et al. (2009) climatology may contribute to the discrepancy, particularly given the heterogeneous nature of polar Southern Ocean phytoplankton blooms and other processes controlling pCO_2^{sw} (Moore and Abbott 2000; Doney et al. 2003; Arrigo et al. 2008a,b).

In the North Atlantic (49°–80°N), CESM1 predicts an annual-mean pCO_2^{sw} that is comparable to the observations,
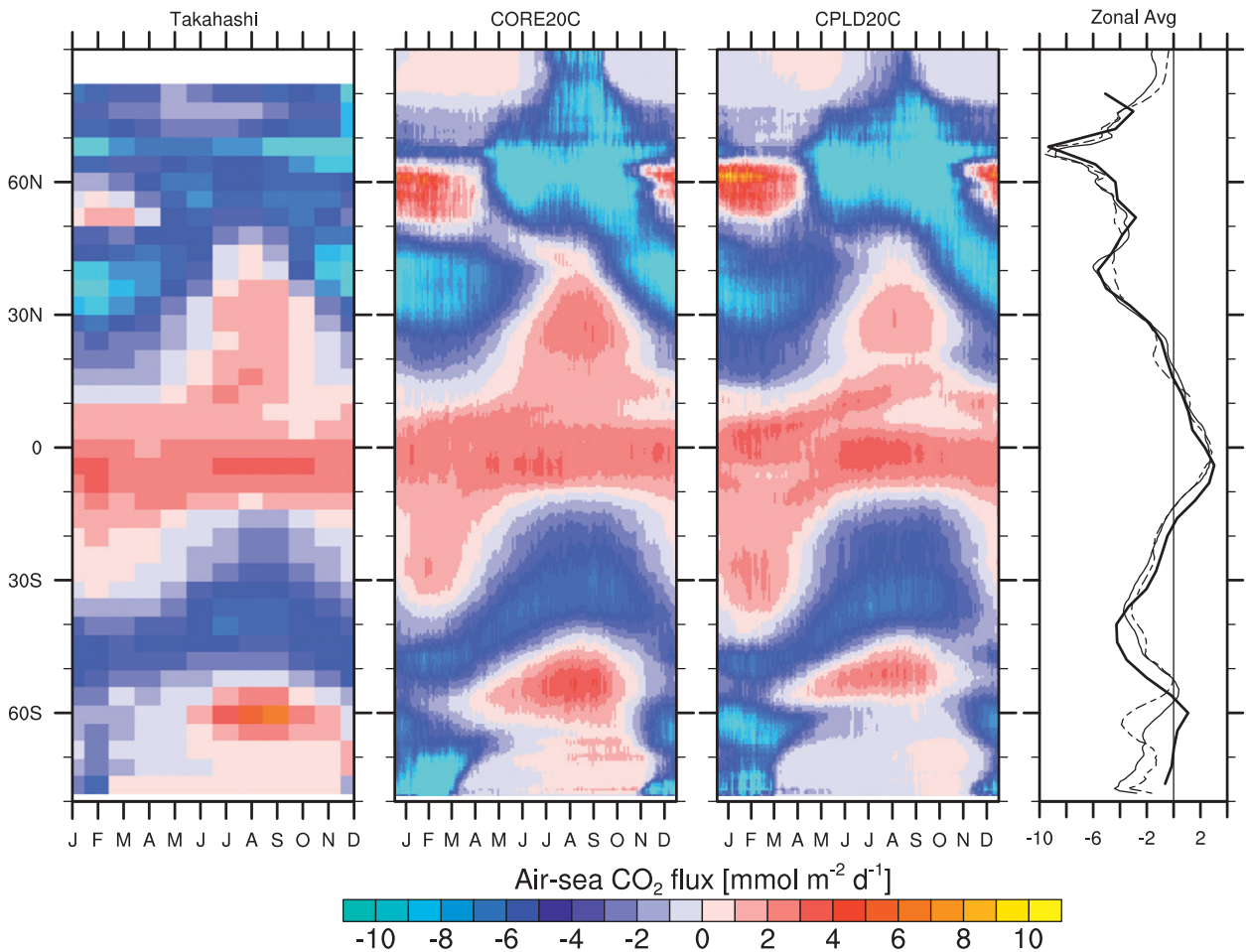
FIG. 3. Sea–air CO_2 flux from the monthly climatology of Takahashi et al. (2009), CORE20C, and CPLD20C (negative = ocean uptake). (right) The annual zonal-mean flux from observations (thick solid), CORE20C (thin solid), and CPLD20C (dashed).

but the amplitude of the seasonal cycle in the model is ~5-fold larger. Summer CO_2 drawdown may be overestimated by the model; high-chlorophyll biases in this region indicate that the magnitude of the simulated Arctic phytoplankton bloom is too strong (Moore et al. 2013). Winter maximum mixed layer depths are too deep in this region (Danabasoglu et al. 2012; Moore et al. 2013), likely leading to excessive DIC entrainment into surface waters. Data sparsity may also contribute to this discrepancy, resulting in an aliased seasonal cycle in the observations.

While the amplitude of the high-latitude seasonal cycle in pCO_2^{sw} is generally much larger than interannual variability (at the large scales reflected by regional means), the opposite is true in the tropics (Fig. 2). Much of the interannual variability in carbon cycling in this region is related to ENSO, discussed in detail below.

c. Air–sea fluxes

Figure 3 shows the seasonal cycle in zonally averaged sea–air flux from the Takahashi et al. (2009) monthly

climatology, CORE20C, and CPLD20C. Overall, there is good agreement between the model and the observations: outgassing in the tropics throughout the year and a strong seasonal cycle in sea–air flux at high latitudes. In terms of the annual-mean flux (Fig. 3, far right), CESM closely matches the ΔpCO_2-based climatology, except in the Southern Ocean.

In both model configurations, contemporary CO_2 uptake is weaker than ΔpCO_2-based flux estimates between about 40° and 55°S; whereas south of 60°S the models show stronger uptake (Fig. 3, far right)—consistent with the biases in ΔpCO_2 (Fig. 1). In the CORE-forced integration, this results in compensating biases, yielding close correspondence with observationally based zonally integrated flux estimates south of 44°S (Fig. 4); however, coupled model CO_2 uptake in this region is about 0.15 PgC yr^{-1} greater than in CORE20C. Much of this discrepancy results from anomalous CO_2 uptake in CPLD20C around 60°S. Southern Hemisphere sea ice coverage is far too extensive in CPLD20C; the total sea
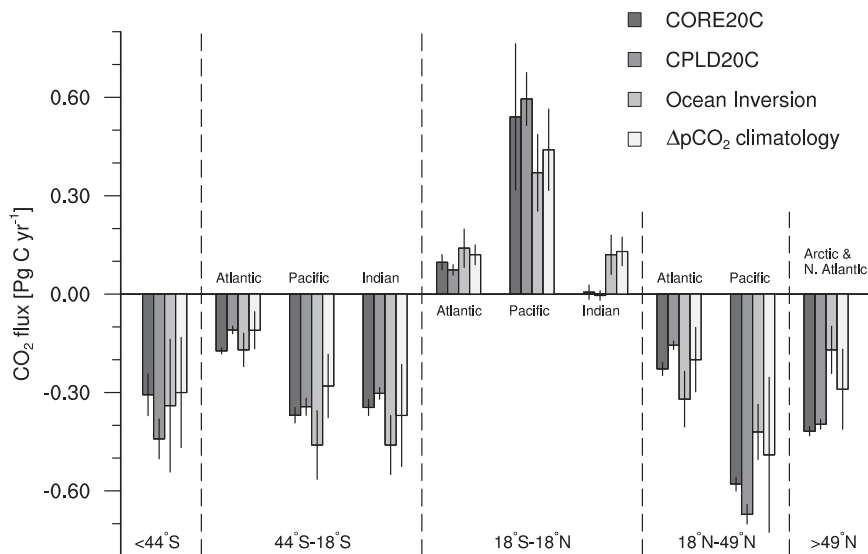
FIG. 4. Zonally integrated contemporary sea–air CO_2 fluxes by ocean basin (negative = ocean uptake). Data from CORE20C and CPLD20C are the mean fluxes over the period 1990–2000. Also shown are the ocean inversion estimates from Gruber et al. (2009) and ΔpCO_2-based estimates from Takahashi et al. [2009; regional averaging and error computation done by Gruber et al. (2009)]. For the observationally based estimates, error bars are taken from Gruber et al. (2009); the model error bars show $\pm 1\sigma$ for the 11-yr period.

ice area is consistently about 62% ($\sim 4.0 \times 10^6\,km^2$) greater than satellite observations over the seasonal cycle (Landrum et al. 2012). This is likely due to westerly winds in the coupled model that are stronger than observed (Danabasoglu et al. 2012); sea ice coverage in CORE20C, by contrast, is reasonable. As a result of extensive sea ice in CPLD20C, austral summer CO_2 uptake south of 60°S is weakened and shifted northward relative to that in CORE20C (Fig. 3). However, in spite of stronger Southern Ocean winds in the coupled model, extensive ice cover dampens austral winter outgassing (Fig. 3); thus, on an annual time scale, CPLD20C yields a greater Southern Ocean sink for contemporary CO_2 than CORE20C or the ΔpCO_2-based flux estimates (Fig. 4).

In the tropics, there is close correspondence between modeled and observed zonal-mean fluxes at the global scale (Fig. 3). An examination of zonally integrated fluxes within each basin indicates some regional disparities leading to compensating biases (Fig. 4). The equatorial Pacific in both model configurations has outgassing rates higher than in either observational dataset, while the model outgassing rates are slightly low (but perhaps not significantly) relative to observations in the equatorial Atlantic. The tropical Indian Ocean has sea–air CO_2 flux rates near zero in the model, whereas the observations indicate a source of about 0.1 $PgC\,yr^{-1}$.

Contemporary CO_2 fluxes can be partitioned into preindustrial (natural) and anthropogenic components

(C_{ant}). The Southern Ocean has the greatest zonally integrated uptake of C_{ant} (Fig. 5). The two model configurations return very similar estimates of Southern Ocean C_{ant} uptake, about 0.2 $PgC\,yr^{-1}$ less than the ocean inversion estimates (Fig. 5; Gruber et al. 2009). However, while the estimates of Southern Ocean C_{ant} uptake are similar between the two models, the Southern Ocean in the CORE-forced integration has stronger outgassing of natural CO_2. Southern Ocean uptake of C_{ant} is comparable between the two model configurations; thus, weaker contemporary CO_2 uptake in the CORE-forced integration is a result of stronger preindustrial outgassing (Fig. 4). However, despite being stronger than in the coupled integration, preindustrial outgassing in CORE1850 is still about 0.2 $PgC\,yr^{-1}$ lower than ocean inversion estimates (Fig. 5). This is consistent with generally weak ventilation and vertical exchange in the CESM models, something seen previously in CCSM3 (Thornton et al. 2009; Wang et al. 2012).

d. Multidecadal pCO_2^{sw} trends

As the ocean absorbs carbon from the atmospheric CO_2 perturbation surface ocean DIC increases, which drives increases in pCO_2^{sw} at a rate that slightly lags pCO_2^{atm}, reflecting vertical mixing and sea–air exchange time scales (Le Quéré et al. 2010). If pCO_2^{sw} increases at the same rate as pCO_2^{atm}, there should be no change in ΔpCO_2. Indeed, global-mean trends in ΔpCO_2 indicate that ocean pCO_2 approximately tracked pCO_2^{atm} in both
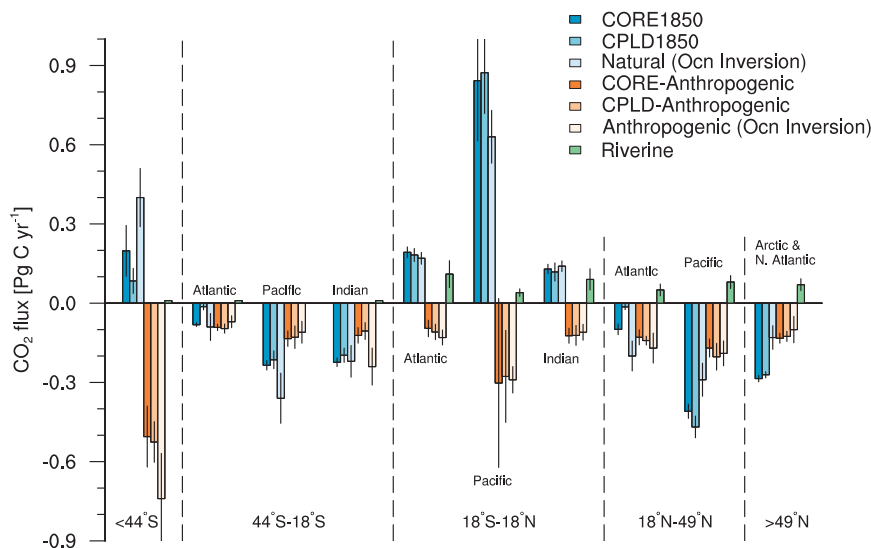
FIG. 5. Zonally integrated sea–air CO_2 flux components by ocean basin (negative = ocean uptake). Bars plotted in blue shades show preindustrial (natural) fluxes, whereas red shades show anthropogenic fluxes. Data from CORE20C and CPLD20C are the mean fluxes over the period 1990–2000. Also shown are the ocean inversion estimates from Gruber et al. (2009). For the observationally based estimates, error bars are taken from Gruber et al. (2009); the model error bars show $\pm 1\sigma$ for the 11-yr period. See Gruber et al. (2009) for further details on the riverine flux contributions.

CORE20C and CPLD20C, yielding weak trend in $\Delta p CO_2$. Over the period 1981–2005 $p CO_2^{atm}$ increased at about 1.59 ppm yr^{-1}; meanwhile, the global-mean $\Delta p CO_2$ trend was -0.017 ppm yr^{-1} in the CORE-forced integration and -0.05 ppm yr^{-1} in the coupled model. Increasingly negative $\Delta p CO_2$ values drive increasing ocean uptake of CO_2.

In spite of weakly negative global-mean trends, regional variability in $\Delta p CO_2$ trends is evident in both model configurations (Figs. 6a,b). The term $p CO_2^{sw}$ increased faster than $p CO_2^{atm}$ in the subtropical Pacific and the Arctic Ocean in CORE20C and CPLD20C. Positive $\Delta p CO_2$ trends are also evident in the subantarctic in CORE20C. Conversely, the North Atlantic and polar Southern Ocean exhibit negative trends in $\Delta p CO_2$ in both model configurations, indicative of surface ocean $p CO_2$ falling behind that of the atmosphere.

Comparison of modeled trends with observationally based trend estimates shows regions of both agreement and disagreement. For instance, Le Quéré et al. (2010) found that $p CO_2^{sw}$ was increasing faster than $p CO_2^{atm}$ in the western tropical Pacific and the subantarctic region of the Southern Ocean; $p CO_2^{sw}$ increased more slowly than $p CO_2^{atm}$ in the North and South Pacific. There is some consistency between these results and trend in CORE20C, although considerable spatial heterogeneity complicates comparisons (Fig. 6). Le Quéré et al. (2010) found that $p CO_2^{sw}$ was increasing faster than $p CO_2^{atm}$ in the North Atlantic, which is not consistent with the

model results. However, McKinley et al. (2011), who examined North Atlantic $p CO_2^{sw}$ trends in observations, found that between 1981 and 2009 North Atlantic $p CO_2^{sw}$ increased uniformly over the region at a rate just below that of $p CO_2^{atm}$. These authors demonstrate that climate variability can cause $p CO_2^{sw}$ trends to deviate from $p CO_2^{atm}$ trends on decadal time scales (see also Thomas et al. 2008), but over the long term (+25 yr), $p CO_2^{sw}$ in the North Atlantic basically tracks $p CO_2^{atm}$.

Metzl (2009) analyzed observations in the Indian Ocean sector of the Southern Ocean (south of 20°S), finding a rate of increase in surface ocean $p CO_2^{sw}$ equivalent to 2.11 ± 0.07 μatm yr^{-1} (1 atm $\equiv 1013.25$ hPa) between 1991 and 2007 (i.e., faster than the respective rise in $p CO_2^{atm}$ of 1.72 μatm yr^{-1}) leading to a positive trend in $\Delta p CO_2$ and weakened uptake. Results from CORE20C show comparable significant increases in $p CO_2^{sw}$ in a similar region; in fact, the Indian Ocean sector of the Southern Ocean appears to have the greatest rate of $p CO_2^{sw}$ increase in the subantarctic.

While $p CO_2^{sw}$ is affected by temperature, which impacts CO_2 solubility, nonthermal (i.e., DIC and alkalinity concentrations) factors dominate $p CO_2^{sw}$ variability. Figures 6e,f shows the trend in $p CO_2^{sw}$ between 1980 and 2005 that is attributable to trends in SST; subtracting temperature-induced changes in $p CO_2$ from the total change provides a measure of the nonthermally induced $p CO_2^{sw}$ change (Figs. 6g,h). In both model configurations, the thermally

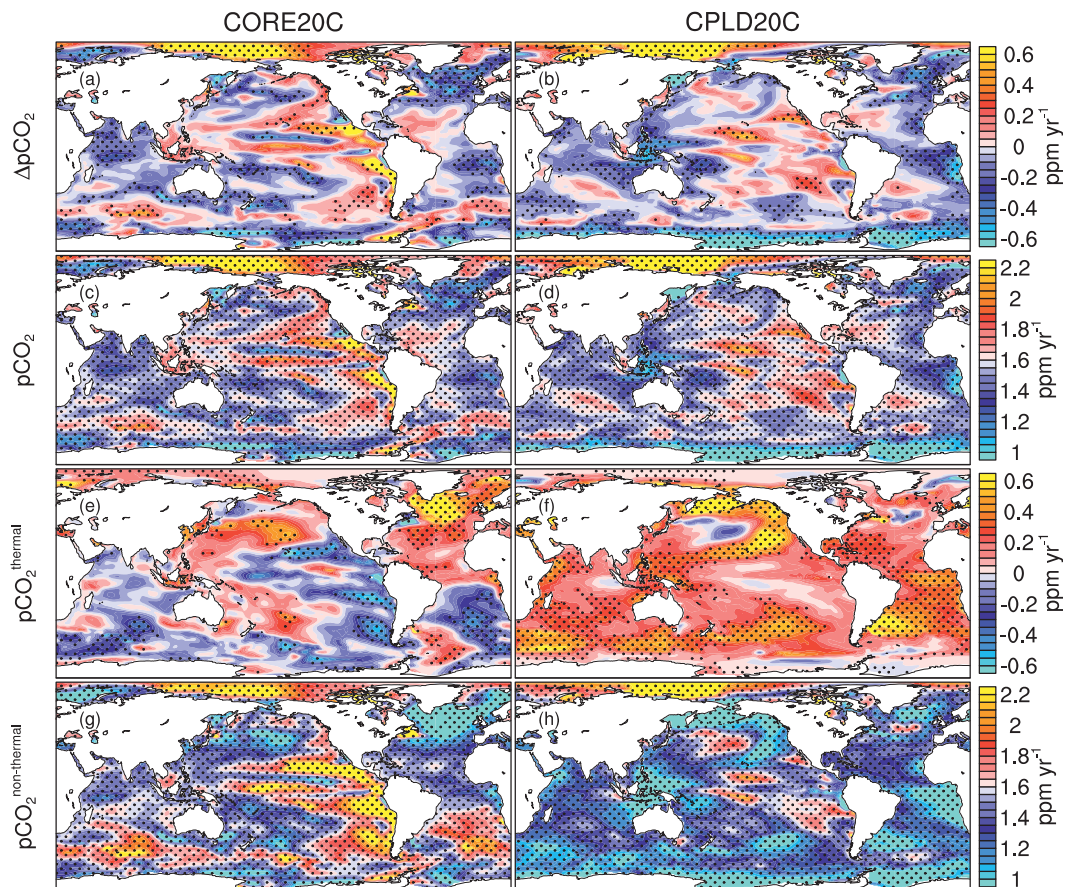FIG. 6. (a),(b) Trends in $\Delta p CO_2$ ($\Delta p CO_2 = p CO_2^{sw} - p CO_2^{atm}$) between 1981 and 2005. (c),(d) Trends in $p CO_2^{sw}$. (e),(f) Trends in $p CO_2^{sw}$ driven by changes in sea surface temperature over the same period (Takahashi et al. 2002). (g),(h) Trends in $p CO_2^{sw}$ not driven by temperature (over most of the globe this component is mostly driven by changes in dissolved inorganic carbon and secondarily affected by changes in alkalinity, salinity, and freshwater; these latter effects can be locally important). (left) Results from CORE20C and (right) CPLD20C. Note the differing color bars: for the first and third rows, the color bar is centered on zero; in the second and bottom row, it is centered on 1.6 ppm yr^{-1}, which is the rate at which $p CO_2^{atm}$ increased over the period shown. Stippling denotes significance at the 95% confidence level.

induced portion of the $p CO_2^{sw}$ trend is the smaller component, which is consistent with observations over the same period (e.g., McKinley et al. 2011). Notably, however, the thermal component in the coupled model is stronger and more uniformly positive than in the CORE-forced integrations (Figs. 6c,d). This is due to greater trends in SST in the coupled model, in which twentieth-century warming is about 0.4°C in excess of that observed (Gent et al. 2011). The spatial patterns of warming-induced $p CO_2^{sw}$ trends in CORE20C and CPLD20C are not similar. The North Atlantic stands out as a large coherent region of significant warming-related trends in CORE20C, a feature absent from CPLD20C (Figs. 6e,f). The coupled model exhibits significant warming-induced trends in the subtropical gyres and subantarctic (Fig. 6f).

e. Multidecadal CO$_2$ flux trends

Sea–air flux in the steady-state preindustrial ocean is thought to have been about $+0.5 \, \mathrm{PgC \, yr^{-1}}$ because of the outgassing of carbon inputs from rivers (Fig. 5; Gruber et al. 2009). Since CESM1(BGC) does not currently represent riverine carbon contributions, the long-term mean of global-scale natural CO$_2$ fluxes is near zero in both model configurations (Figs. 7a,b). The experimental design of the CORE-forced integrations precludes substantive inferences about trends prior to 1948; however, we note that the long-term trends in sea–air fluxes in CORE1850 are near zero (Table 3).

There is a moderate positive (outgassing) trend in natural CO$_2$ flux over 1970–2005 in the CORE-forced integration (Fig. 7a; Table 3). Since this trend is greater
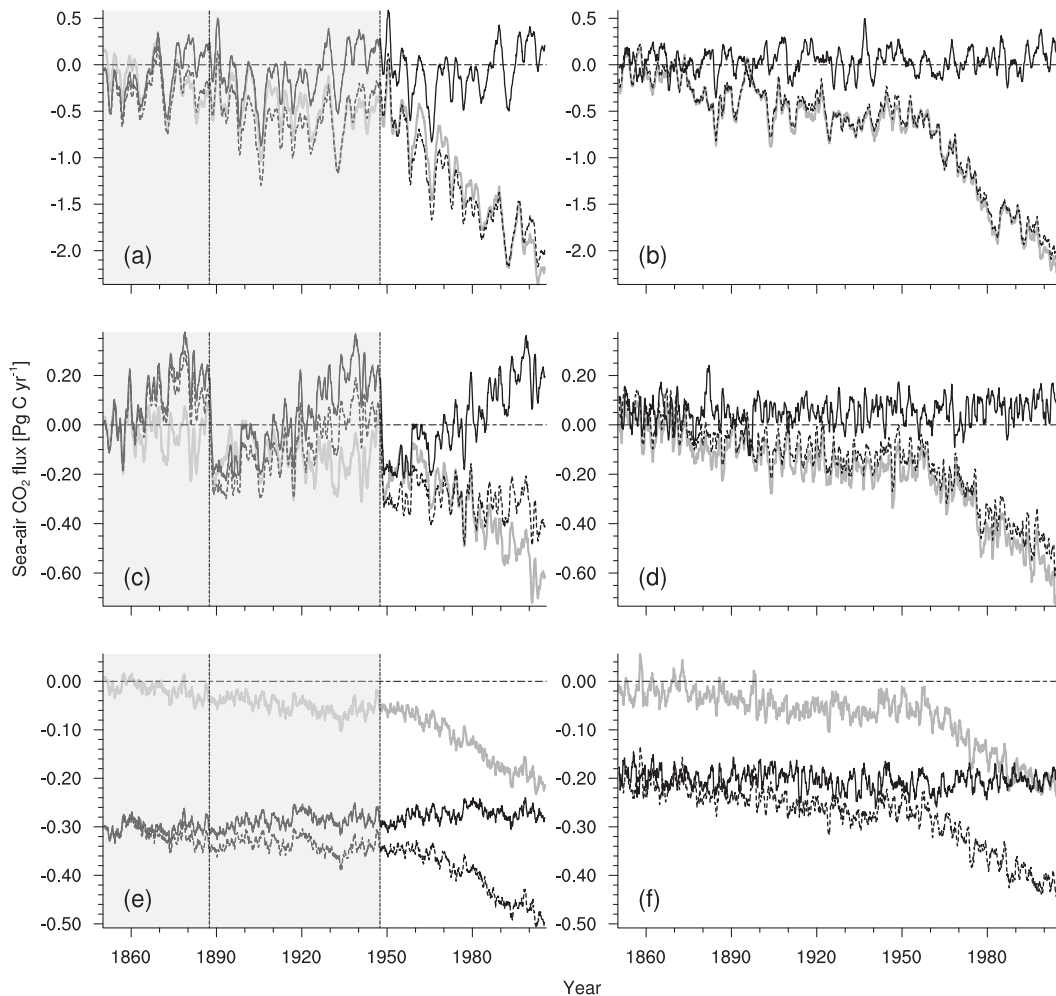
FIG. 7. Sea–air CO_2 fluxes (negative = ocean uptake) in the (left) CORE-forced and (right) coupled integrations. (a),(b) Globally integrated fluxes, (c),(d) Southern Ocean (south of 44°S), and (e),(f) North Atlantic (36°–76°N). In each panel, the solid black line shows the 1850 control (preindustrial fluxes), the dashed line shows the twentieth-century transient (contemporary), and the gray line shows the difference (after removal of interannual variability in preindustrial fluxes): anthropogenic CO_2. The CORE forcing applies to the period 1948–2007, but was recycled (see methods) to span the period 1850–2007. Vertical lines in panels (a),(c), and (e) show the beginning of each 60-yr forcing cycle; climate-driven variability and trends prior to 1948 are not real, thus this period is grayed out.

in the CORE-forced integration than in the coupled model, the trajectories of globally integrated contemporary and C_{ant} fluxes are more similar in the coupled model (Fig. 7b; Table 3).

The Southern Ocean and North Atlantic are two key regions for oceanic carbon uptake. These regions had the greatest trends in contemporary, and hence C_{ant}, uptake over the globe (Table 3). The trends in North Atlantic sea–air CO_2 flux components are similar between the models (Table 3; Figs. 7e,f) and, consistent with the flux trend, ΔpCO_2 is decreasing (becoming more negative; Figs. 6a,b).

The behavior of the models in the Southern Ocean is markedly different. In particular, there are strong trends

toward outgassing of natural CO_2 evident in the CORE-forced integration over the forcing period (1948–2005); the coupled model has only very weak trends (Figs. 7c,d; Table 3). The trends in the CORE-forced integration are clearly a manifestation of the forcing, not model drift: the last three 60-yr natural CO_2 flux time series corresponding to the successive forcing cycles (i.e., model years 61–120, 121–180, and 181–240) are nearly identical.

Southern Ocean CO_2 flux trends in the CORE-forced integrations are attributable to intensification of the westerly winds. Stronger westerlies accelerate the Antarctic Circumpolar Current, driving enhanced upwelling of DIC at the Antarctic divergence in the model (e.g.,

TABLE 3. Linear temporal trends in sea–air flux of natural anthropogenic (Anthr.) and contemporary (Contemp.) CO_2. In each column, the values for 1) CORE-forced and 2) coupled integrations are separated by a comma. Trends over the period 1850–2005 from the CORE-forced integrations should be interpreted as model drift. Units are $mmol\,m^{-2}\,yr^{-2}$. "Ns" denotes trends not significant at the 95% confidence level.

Region	1850–2005 natural	1970–2005 natural	Anthr.	Contemp.
Global	ns, 0.06	2.78, ns	−4.47, −5.76	−7.25, −6.24
Southern Ocean <58°S	ns, −0.09	9.38, ns	−7.12, −13.50	−16.50, −13.98
Southern Ocean >58°S	ns, 0.40	ns, 2.45	ns, −8.48	−11.83, −10.93
South midlatitude Pacific	ns, 0.16	1.07, ns	−3.33, −2.63	−4.40, −3.39
West tropical Pacific	ns, 0.29	ns, ns	ns, −3.38	−5.22, −4.22
East tropical Pacific	ns, −0.57	ns, −2.43	ns, ns	ns, ns
North Pacific	0.25, 0.23	ns, ns	−4.25, −3.97	−4.28, −5.96
South midlatitude Indian Ocean	ns, ns	ns, ns	−4.01, −5.73	−5.55, −5.23
Tropical Indian Ocean	ns, ns	3.04, ns	−2.51, −6.43	−5.55, −6.80
South midlatitude Atlantic	0.40, 0.14	2.57, −0.31	−3.65, −6.81	−6.22, −6.50
Tropical Atlantic	ns, 0.12	ns, ns	−4.50, −7.22	−4.78, −7.57
North midlatitude Atlantic	0.32, 0.54	ns, ns	−6.70, −6.05	−7.03, −7.71
North high-latitude Atlantic and Arctic	ns, −0.95	ns, ns	−12.33, −8.53	−10.25, −6.74

Lovenduski et al. 2008; Russell et al. 2006). Furthermore, since the ACC is topographically constrained to between about 50° and 55°S, shifting the winds poleward yields closer alignment of the wind forcing with the ACC further enhancing Ekman pumping (Toggweiler and Russell 2008). Trends in both the strength and position of the Southern Hemisphere westerlies are evident in the CORE forcing (Figs. 8a,b). Indeed, net advection of
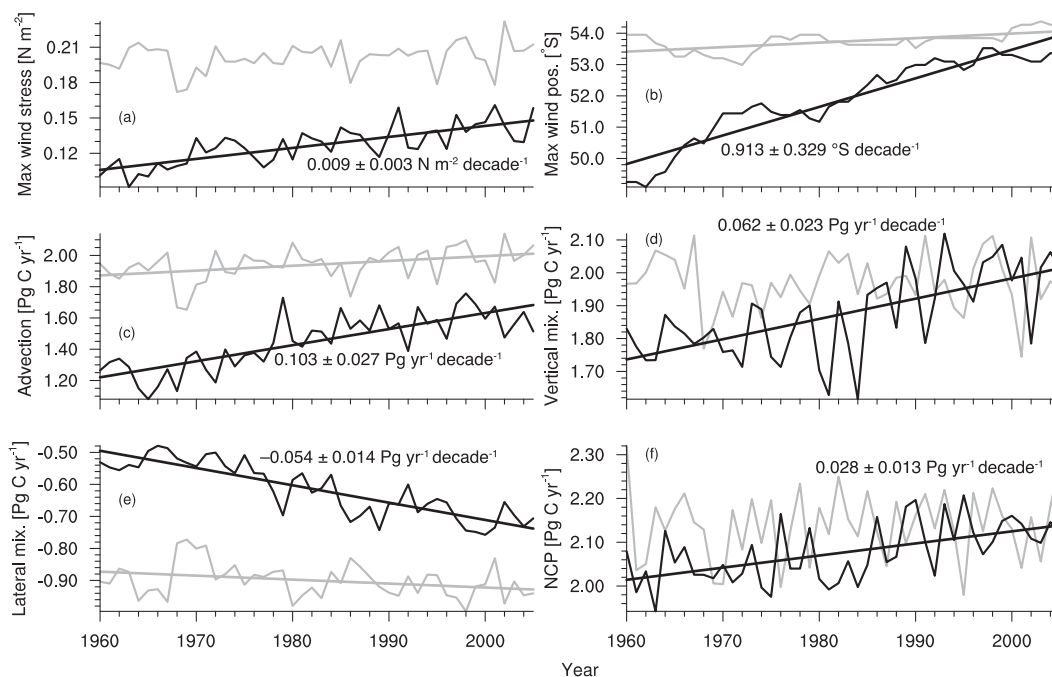

FIG. 8. Southern Ocean trends from the CORE-forced (black lines) and coupled (gray lines) 1850 CO_2 integrations for the period corresponding to 1960–2005. (a) Maximum zonal-mean zonal wind stress in the Southern Hemisphere. (b) Meridional position of maximum zonal-mean wind stress. Terms in the mass balance of DIC in the upper 100 m of the Southern Ocean (south of 44°S): (c) net horizontal and vertical advection (at resolved scales), (d) vertical diffusion (parameterized mixing), (e) eddy-induced lateral mixing, and (f) net community production (biological consumption of DIC minus respiration or release of DIC). The data in (b) were smoothed with a 10-yr running mean to reduce year-to-year noise. Trend lines show regressions significant at the 95% level; the slope is noted in each panel. Coefficients of determination (r^2) for the CORE regressions are (a) 0.593, (b) 0.897, (c) 0.630, (d) 0.421, (e) 0.743, and (f) 0.319. No significant trends were evident in the coupled model.
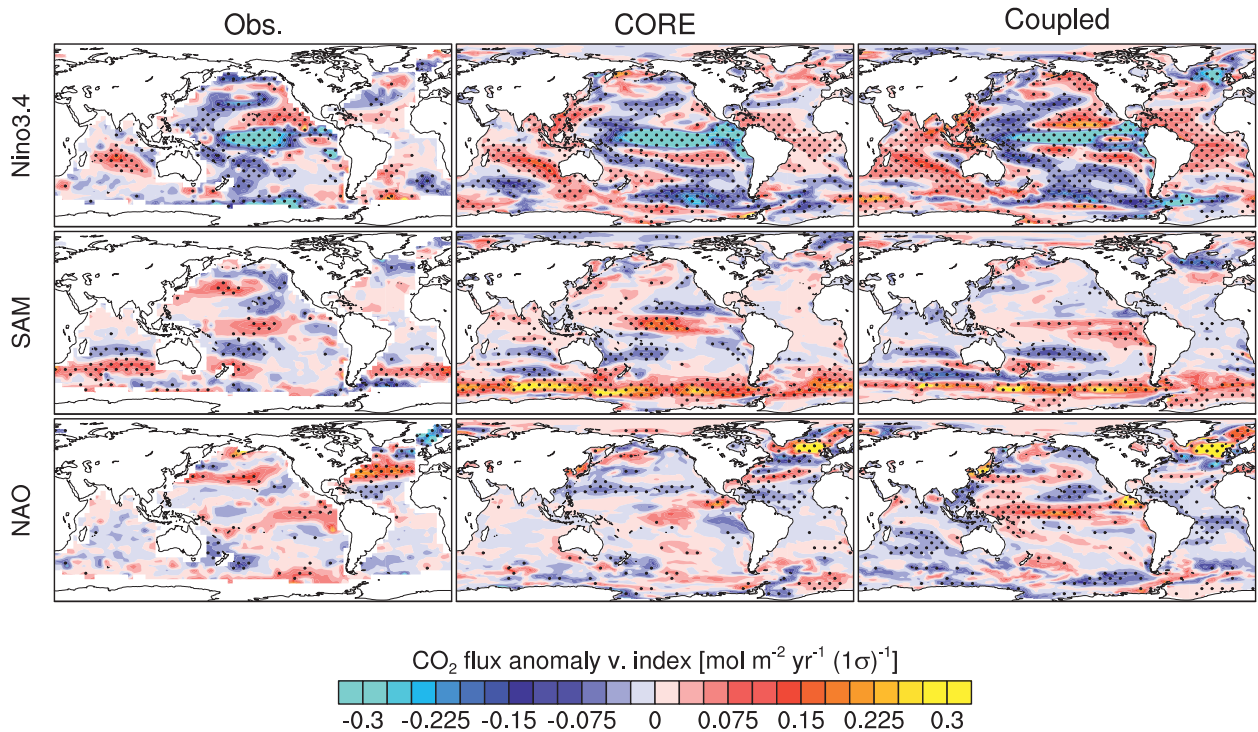
FIG. 9. Regression of sea–air CO_2 flux anomalies vs the standardized (top) Niño-3.4 index, (middle) SAM, and (bottom) NAO. (left) Observationally based data of Park et al. (2010). (center) The ocean-ice hindcast. (right) The coupled model results. Stippling denotes significance at the 95% confidence limit.

DIC into the upper 100 m of the Southern Ocean increases between 1960 and 2005 in the CORE-forced integration (Fig. 8c), which is the dominant mechanism driving a positive trend in natural CO_2 outgassing.

Notably, there are no significant trends in the zonal-mean zonal wind stress or carbon budget components in the coupled model (Fig. 8). Some of the twentieth-century CCSM4 ensemble members show stronger

TABLE 4. Mean spatially integrated and areal contemporary sea–air CO_2 fluxes and variability (1σ of annual mean) by region for the period 1990 and 2005. In each column, the first number is the Park et al. (2010) estimate, the last two numbers are CORE20C and CPLD20C, respectively. Note that the numbers reported here differ from those in Table 1 of Park et al. (2010) because of averaging over a different time period and exclusion of the Southern Ocean sea ice zone. "Na" denotes values that are not available.

	Mean (PgC yr^{-1})	Variability (PgC yr^{-1})	Mean (mol m^{-2} yr^{-1})	Variability (mol m^{-2} yr^{-1})	Area[a] (10^6 km^2)
Global[b]	−1.15, −1.59, −1.55	0.12, 0.19, 0.15	−0.31, −0.40, −0.39	0.03, 0.05, 0.04	326.30, 332.39
Southern Ocean <58°S	na, −0.18, −0.28	na, 0.03, 0.03	na, −0.61, −0.96	na, 0.10, 0.09	23.86, 24.31
Southern Ocean >58°S	−0.26, −0.15, −0.17	0.02, 0.05, 0.05	−0.68, −0.33, −0.38	0.05, 0.12, 0.10	32.34, 38.03
South midlatitude Pacific	−0.30, −0.36, −0.34	0.02, 0.02, 0.02	−0.64, −0.81, −0.75	0.03, 0.05, 0.05	38.91, 37.61
West tropical Pacific	0.06, −0.12, −0.17	0.04, 0.07, 0.03	0.16, −0.30, −0.44	0.10, 0.17, 0.08	30.39, 32.81
East tropical Pacific	0.53, 0.65, 0.75	0.07, 0.14, 0.07	1.30, 1.58, 1.81	0.17, 0.33, 0.17	33.59, 34.57
North Pacific	−0.47, −0.56, −0.66	0.02, 0.02, 0.03	−0.99, −1.04, −1.22	0.05, 0.04, 0.05	39.98, 45.03
South midlatitude Indian Ocean	−0.38, −0.34, −0.31	0.01, 0.02, 0.03	−1.16, −1.07, −0.95	0.04, 0.07, 0.09	27.10, 26.73
Tropical Indian Ocean	0.12, −0.00, −0.01	0.01, 0.02, 0.03	0.38, −0.00, −0.04	0.02, 0.06, 0.08	25.26, 30.85
South midlatitude Atlantic	−0.12, −0.17, −0.11	0.01, 0.01, 0.01	−0.54, −0.75, −0.50	0.05, 0.04, 0.07	19.43, 18.82
Tropical Atlantic	0.11, 0.09, 0.07	0.01, 0.02, 0.02	0.45, 0.32, 0.23	0.05, 0.07, 0.08	21.13, 24.21
North midlatitude Atlantic	−0.20, −0.23, −0.16	0.02, 0.02, 0.02	−0.78, −0.84, −0.58	0.06, 0.08, 0.06	20.87, 22.57
North high-latitude Atlantic[c]	−0.23, −0.39, −0.38	0.04, 0.01, 0.01	−2.58, −1.99, −1.93	0.42, 0.06, 0.07	11.32, 16.29

[a] The first number in this column is the Park et al. (2010) area, while the second is from CESM; they differ as a result of differing *resolution*.
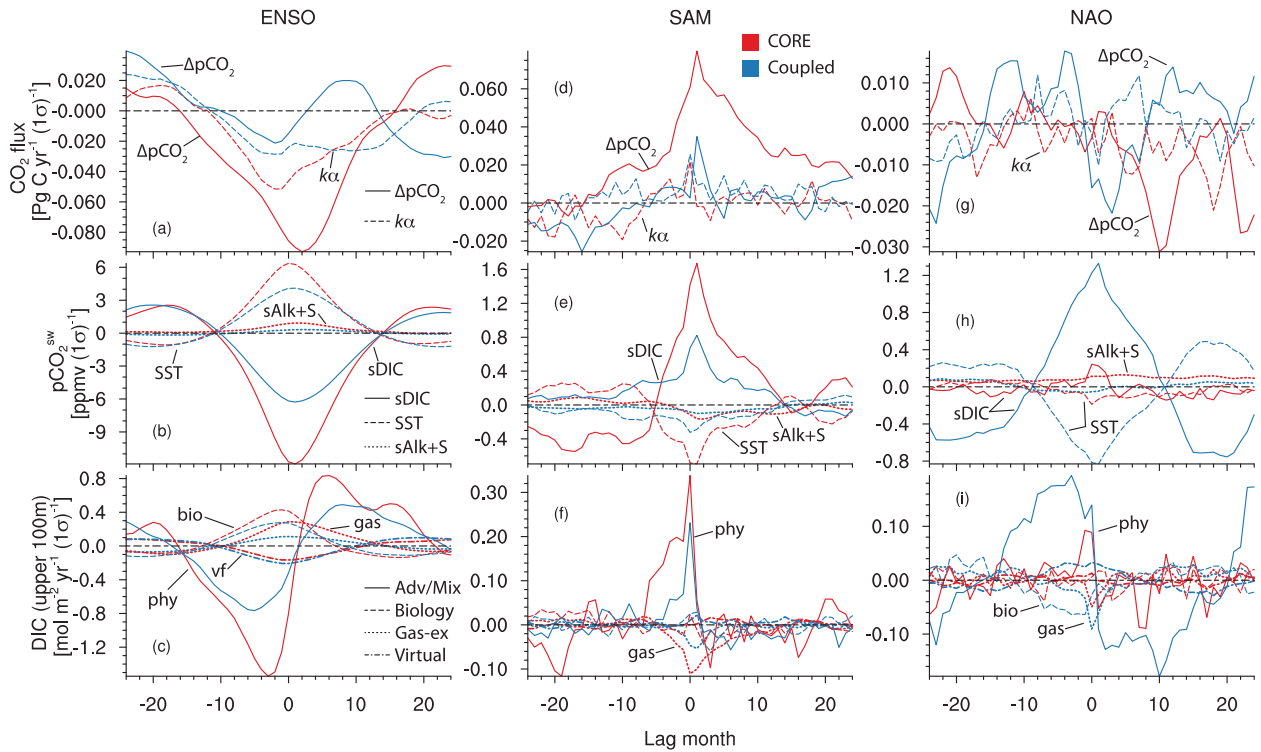[b] Excluding area south of 60°S and Arctic above 80°N.
[c] <80°N.

FIG. 10. Lagged regressions of linear Taylor series components of sea–air (top) CO_2 flux, (middle) surface ocean pCO_2, and (bottom) upper ocean dissolved inorganic carbon inventory against climate indices: (left) Niño-3.4, (center) SAM, and (right) NAO. Red lines show results from the CORE-forced integrations; blue show coupled results. The legend for each row is shown in the plot on the far left. See text for description of various terms.

trends in zonal-mean zonal wind but none as strong as the reanalysis-based CORE data (Weijer et al. 2012).

Given that enhanced wind-driven upwelling drives the positive trend in sea–air flux in the CORE-forced integration, one might expect greater outgassing in the coupled model-mean state since the coupled model has greater wind stress over the entire 1960–2005 period (Fig. 8a). Outgassing of natural CO_2 is weaker in the coupled model, however, which is due to a different DIC distribution: Southern Ocean surface sDIC is greater and the vertical gradient in sDIC is stronger in the CORE-forced run relative to the coupled model (Fig. S2 of the supplementary material). Notably, both model configurations underestimate the vertical gradient in sDIC compared to the observationally based climatology, with markedly different structure in the sDIC profile between about 300 and 1200 m (Fig. S2).

Transport of DIC by the Eulerian-mean circulation and turbulent diffusion across 100 m are the dominant components causing DIC to increase in Southern Ocean surface waters in CORE20C (Figs. 8c,d). Notably, eddy-induced lateral advection and isopycnal mixing (i.e., parameterized mesoscale mixing) work to oppose resolved advection; this effect becomes more negative as winds increase (Fig. 8e). This behavior is consistent with

theory, which suggests that the eddy-induced overturning should compensate increases in the Eulerian-mean overturning (Marshall and Radko 2003). The degree to which compensation should occur is uncertain, however, and may be too weak in the model. Nevertheless, the variable eddy-induced advection coefficient permits eddy-induced overturning to accelerate in opposition to the mean flow and partially compensate for increases in wind-driven overturning (Lovenduski et al. 2013).

The final term in the Southern Ocean DIC budget is export production (Fig. 8f), which is a net sink for DIC in the upper ocean. The magnitude of this sink increases in the CORE-forced runs as greater rates of upwelling supply additional nutrients to the surface layer.

f. Interannual variability of sea–air fluxes

In this section, we examine the mechanisms forcing climate-driven variability in CO_2 fluxes on interannual time scales. Our analysis is focused on three dominant modes of climate variability: ENSO, SAM, and NAO, which have a strong influence over ocean physical dynamics and sea–air CO_2 flux. A key question is whether the coupled model can reproduce the biogeochemical effects related to these modes of variability.
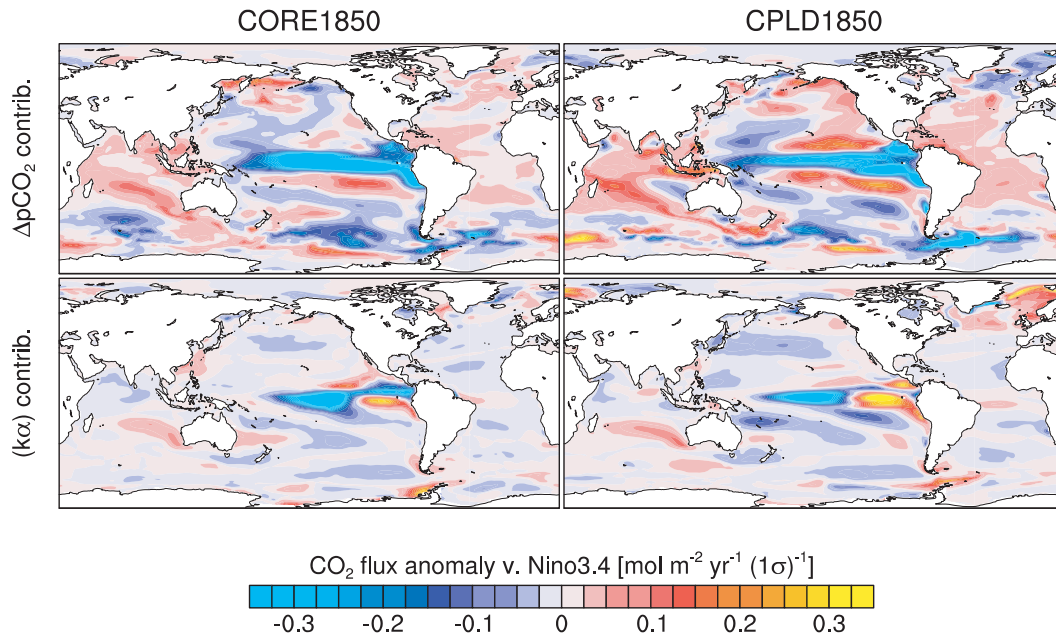
FIG. 11. Regression of sea–air CO_2 flux anomaly components from the (left) ocean-ice hindcast and (right) coupled model vs the standardized Niño-3.4 index (Trenberth 1997).

ENSO is the dominant mode of climate variability driving interannual variability in globally integrated sea–air CO_2 fluxes. During an El Niño event, upwelling of DIC-rich waters in the central and eastern equatorial Pacific is diminished as a result of weakened trade winds. This reduces outgassing locally (Feely et al. 1999; Chavez et al. 1999); furthermore, physical mechanisms in the ocean and atmosphere propagate ENSO-related variability over much of the globe (Wang and Schimel 2003).

In CESM1, a positive ENSO state is characterized by diminished outgassing (order $-0.3\,\mathrm{mol\,m^{-2}\,yr^{-1}}$) in the central equatorial Pacific, a somewhat weaker response of the same sign in the southern Pacific and Atlantic basins and anomalous outgassing over much of the remaining tropics (Fig. 9). This pattern has some similarity to that present in the observationally based reconstruction of Park et al. (2010); however, the spatial extent of anomalous uptake in the central equatorial Pacific is greater in the model, and the degree of anomalous outgassing elsewhere in the tropics is also greater, particularly in the coupled configuration. The counteracting effect of anomalous outgassing beyond the eastern equatorial Pacific weakens the global ENSO-related variability in the coupled model (Fig. 9). Global sea–air fluxes in the hindcast simulation have greater variability than is evident in the Park et al. (2010; Table 4) reconstruction, which may be due to the coarser resolution of the observational climatology (note that Table 4 presents contemporary sea–air CO_2 fluxes).

In the CORE-forced integration, changes in ΔpCO_2 dominate the CO_2 flux response to ENSO variability (solid lines, Fig. 10a). This effect is about double that resulting from reductions in the piston velocity (red dashed line, Fig. 10a), although the influence of piston velocity anomalies are comparable to ΔpCO_2 in the central Pacific (Fig. 11). In the coupled model, by contrast, the two components of the flux response are quite similar (at zero lag), and the combined overall flux response (blue lines, Fig. 10a) is weaker and out of phase with the CORE results.

The pCO_2^{sw} response to ENSO can be further decomposed into driving mechanisms. In the equatorial Pacific, there is a competition between warmer SSTs driving pCO_2^{sw} up and reduced DIC driving it down (Fig. 12). The SST and DIC effects on pCO_2^{sw} are both greater in magnitude in the CORE-forced run than in the coupled model; the DIC effect dominates in both configurations but to a greater extent in the hindcast (Fig. 10b). Physically mediated DIC fluxes (vertical advection and mixing) are the primary terms controlling ENSO-related variability (solid lines, Fig. 10c). The coupled model response is weaker because of compensating increases in upwelling—particularly in the eastern Indian Ocean, as well as the North and South Pacific—that are more pronounced than in the CORE-forced run (Fig. 13).

In addition to ENSO, the SAM also strongly influences sea–air fluxes at the global scale. A positive phase of the SAM is associated with a poleward shift and
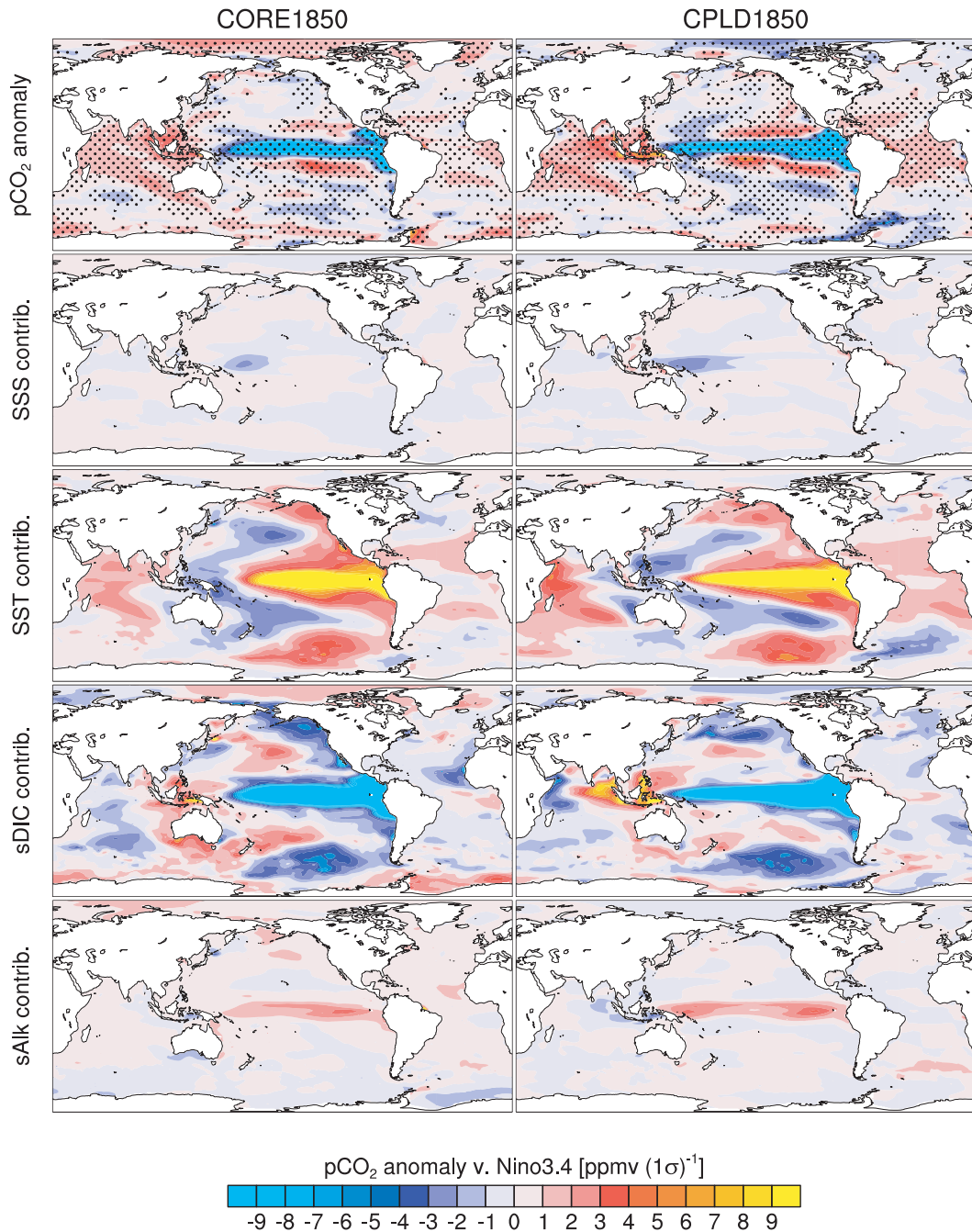
FIG. 12. Regression of surface ocean $p\mathrm{CO}_2$ anomalies and components from the (left) ocean-ice hindcast and (right) coupled model vs the standardized Niño-3.4 index (Trenberth 1997). (top) Stippling denotes significance at the 95% confidence limit; no significance metric is shown on the plots for the components.

intensification of the Southern Hemisphere westerly wind field (Thompson and Solomon 2002), which leads to enhanced DIC upwelling and CO_2 outgassing (Lovenduski et al. 2007; Wang and Moore 2012). Similar to the case with ENSO, the coupled model predicts an overall spatial structure (Fig. 9) and temporal evolution (Fig. 10d)

of SAM-related CO_2 flux anomalies that is similar to the CORE-forced integration; however, the magnitude of the globally integrated CO_2 flux response is weaker. The spatial pattern of the SAM CO_2 flux response in the model bears some similarity to the observational reconstructions in the central Pacific, particularly in the

DIC inventory anomaly v. Nino3.4 [mol m^{-2} yr^{-1} (1σ)$^{-1}$]
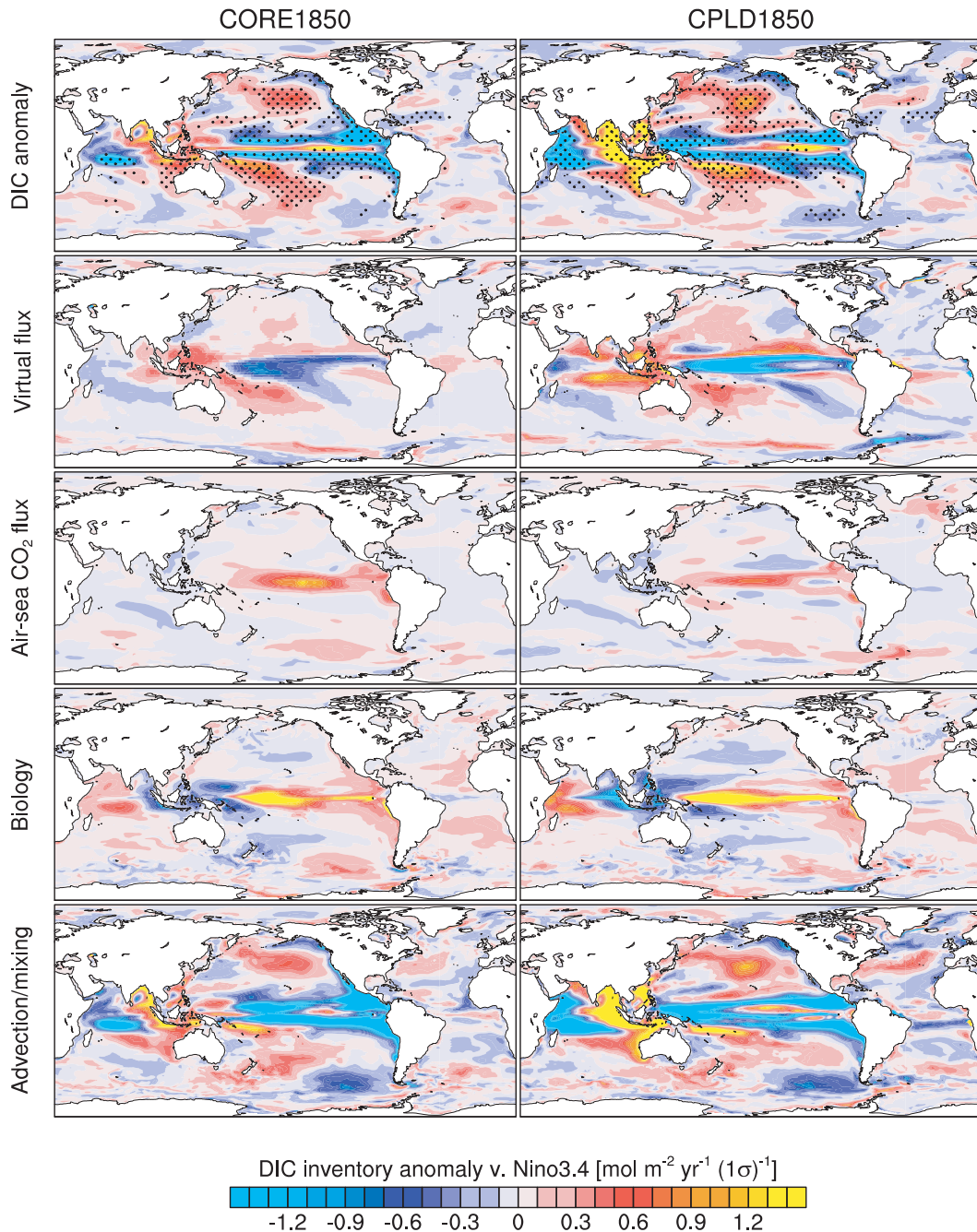
-1.2   -0.9   -0.6   -0.3   0   0.3   0.6   0.9   1.2

FIG. 13. Regression of upper-100-m DIC inventory anomalies and components from the (left) ocean-ice hindcast and (right) coupled model vs the standardized Niño-3.4 index (Trenberth 1997). (top) Stippling denotes significance at the 95% confidence limit; no significance metric is shown on the plots for the components.

CORE-forced integration, but is markedly different in the Southern Ocean (Fig. 9). The SAM-related pCO$_2^{sw}$ response is dominated by DIC anomalies (solid line, Fig. 10e) and driven by anomalous advection and mixing of DIC into the surface ocean (solid line, Fig. 10f). Reduced variability in the coupled model may be related in part to the smaller vertical sDIC gradient in the

Southern Ocean (Fig. S2). In the CORE-forced integration, La Niña–like patterns in the equatorial Pacific are associated with the SAM (Fig. 9): cooler SSTs depress pCO$_2^{sw}$, while enhanced upwelling of DIC drives positive pCO$_2^{sw}$ anomalies and net outgassing (Figs. S3–S5 of the supplementary material). Aspects of this spatial pattern are evident in the Park et al. (2010) observations;
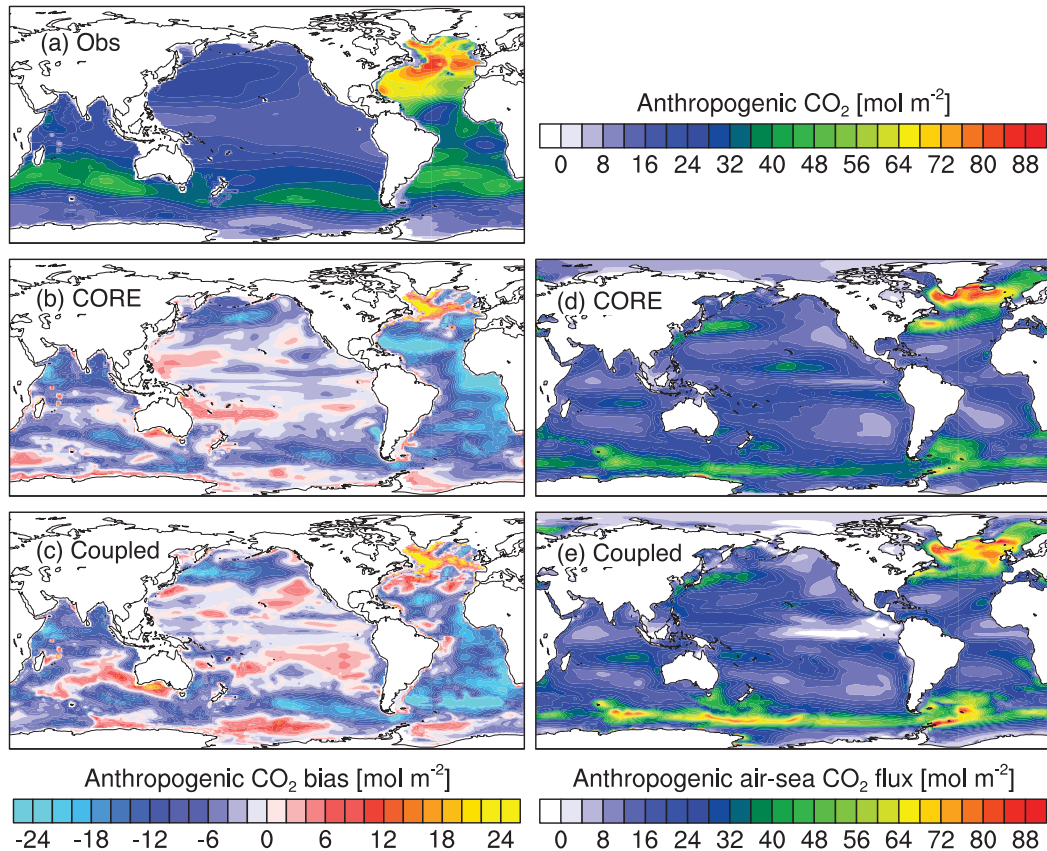
FIG. 14. Column inventory of anthropogenic CO_2 (C_{ant}) from (a) GLODAP (color bar, top right). Model biases in C_{ant} inventory for (b) CORE20C and (c) CPLD20C (color bar, bottom left). Air–sea flux of C_{ant} integrated over 1850–1995 in (d) CORE20C and (e) CPLD20C (note: positive equals uptake in this case).

a notable difference between these and the model, however, is that anomalous SAM-related outgassing is shifted equatorward in the observations (Fig. 9). Since Park et al. (2010) did not provide data poleward of about 60°S, these data cannot be used to evaluate the model in this region.

While the NAO has local flux anomalies comparable in magnitude to those induced by ENSO and SAM (Fig. 9), its impact on globally integrated sea–air CO_2 fluxes is weaker (Fig. 10g). In the Park et al. (2010) observational dataset, the NAO is associated with weak anomalous CO_2 uptake in the tropical Atlantic, outgassing in the subtropics through the midlatitudes, and CO_2 uptake poleward (Fig. 9). This pattern is not well reproduced by the models (Fig. 9), in which anomalous vertical advection and mixing, leading to positive DIC anomalies, drive outgassing in the high-latitude North Atlantic (Figs. S6–S8 of the supplementary material) where the observationally based estimates suggest anomalous uptake should occur. The NAO pattern in the North Atlantic is similar between the models; however, the behavior beyond this region is different (Figs. S6–S8). The most pronounced differences occur in the eastern Pacific,

where the coupled model displays a La Niña–like pattern associated with the NAO (Figs. S6–S8).

g. Carbon inventories

Globally, the total oceanic C_{ant} inventory in both CESM model configurations is too low relative to GLODAP (Table 2). Much of this discrepancy is a result of biases originating in the Southern Ocean; in particular, C_{ant} concentrations are too low in what should be northward-flowing Antarctic Intermediate Water (AAIW; $\sigma_\theta \approx 27.3$; Fig. 15). Column inventories of C_{ant} that are too low at midlatitudes (Fig. 14) are attributable to negative biases at intermediate depths (200–1000 m; Fig. 15). Weak Southern Ocean uptake was also a feature of prior model versions (CCSM3; Thornton et al. 2009; Wang et al. 2012). Notably, C_{ant} distributions in the CORE-forced and coupled configurations are similarly biased, in spite of much different winds.

Anthropogenic CO_2 distributions in the Atlantic basin are marked by positive biases in the region of North Atlantic Deep Water (NADW) formation and negative biases over much of the remaining basin (Figs. 14b,c).
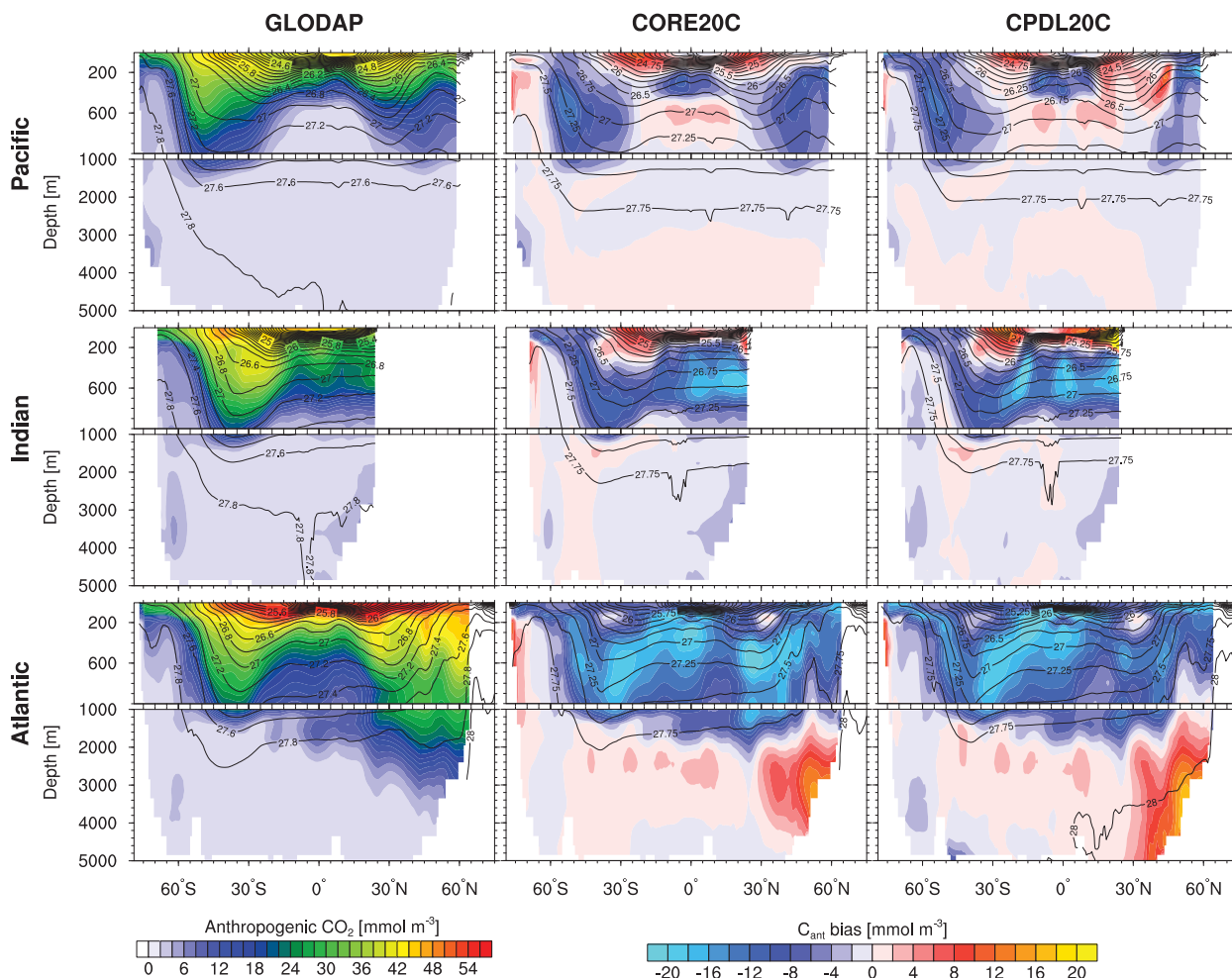
FIG. 15. Zonal-mean anthropogenic CO_2 by ocean basin from (left) GLODAP, and model biases for (center) CORE20C and (right) CPLD20C. Contour lines show potential density surfaces.

Both model configurations display higher C_{ant} concentrations at depth in the North Atlantic than is apparent in the GLODAP climatology. This pattern marks a significant change relative to previous versions of CESM (i.e., CCSM3), in which deep convection in the North Atlantic was displaced too far south, and C_{ant} uptake in NADW was too weak (Thornton et al. 2009; Wang et al. 2012). Changes in North Atlantic uptake dynamics from CCSM3 are explained in part by the new Nordic sea overflow parameterization implemented in CCSM4, which represents unresolved density-driven flows through the Denmark Strait and Faroe Bank Channel, improving the simulation of NADW formation (Danabasoglu et al. 2010, 2012). Poor representation of AAIW contributes to negative biases in the southern part of the Atlantic basin; however, more detailed analysis is required to pinpoint the circulation features contributing to the basinwide bias patterns.

Finally, substantial low biases in the C_{ant} inventories are evident in the North Pacific in both model configurations (Figs. 14b,c). Mode and intermediate water formation in the North Pacific regulate the transfer of CO_2 into the ocean interior (Sabine et al. 2004). The physical processes controlling these water mass transformations are complex (e.g., Nakamura et al. 2006) and not well represented by CESM.

Collectively, the patterns of C_{ant} biases emphasize the importance of physical representations controlling the model's circulation fields (Doney et al. 2004). To emphasize this point, we examine chlorofluorocarbons distributions. While carbon uptake involves both physical and biological processes, oceanic CFC uptake is simply controlled by thermodynamic equilibriums and therefore provides a better indication of physical transport. By examining the partial pressure of CFCs (pCFC) rather than concentrations, the effect of model temperature
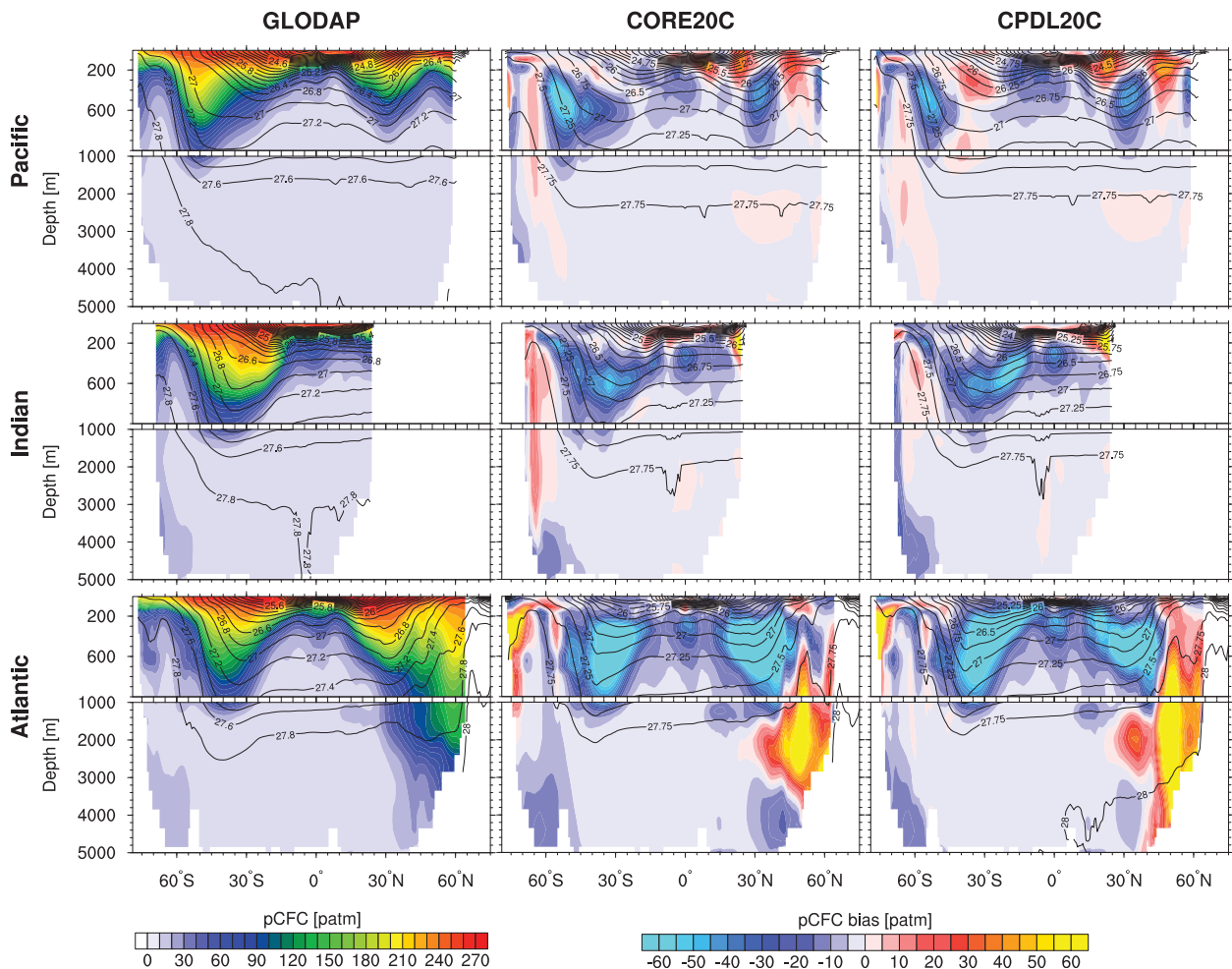
FIG. 16. Zonal-mean partial pressure of CFC-11 (pCFC-11) by ocean basin from (left) GLODAP and model biases for (center) CORE20C and (right) CPLD20C. Contour lines show potential density surfaces.

biases on CFC distributions is minimized. Examination of zonal-mean biases in pCFC-11 (Fig. 16) confirms the inferences regarding circulation biases gleaned from C_{ant} distributions: mode and intermediate water formation in the Southern Ocean is too weak (Weijer et al. 2012); deep convection locally near Antarctica and in the North Atlantic appears too vigorous. We note that small deep-ocean positive C_{ant} biases are ubiquitous in the model (Fig. 15) and greater in magnitude than comparable biases in pCFC-11 at depth (Fig. 16). Some portion of this pattern may be attributable to systematic biases in ΔC^*-derived C_{ant}, which underestimates concentrations at depth (Matsumoto and Gruber 2005; Wang et al. 2012).

The processes affecting mode and intermediate water formation include atmospheric fluxes of buoyancy and momentum. While there is considerable uncertainty in these forcings over the Southern Ocean (e.g., Cerovecki

et al. 2011), the fact that the CORE-forced and coupled integrations have similar biases implies inadequate process representation internal to the ocean model. Indeed, Southern Ocean mixed layer depths are severely too shallow by 30–50 m in the ACC during summer and 100–400 m in winter in both CORE20C and CPLD20C (Danabasoglu et al. 2012; Moore et al. 2013). Mixed layer biases result in weakened uptake, in part through an interaction with the lateral eddy-mixing parameterizations, in which the vertical structure of mixing coefficients depends on boundary layer depth.

5. Summary and conclusions

We have presented an analysis documenting the representation of regional and temporal variability in air–sea fluxes and ocean carbon uptake and storage in two

configurations of CESM1(BGC). Overall, the model captures much of the important spatial and seasonal patterns in pCO_2^{sw}, leading to a generally realistic representation of sea–air fluxes. Low surface alkalinity is an important bias in the model, which contributes to underestimation of oceanic CO_2 uptake associated with a perturbation to atmospheric CO_2.

Modeled temporal trends in surface ocean pCO_2 did not deviate radically from trends in pCO_2^{atm} over the period examined (1981–2005). During this period, pCO_2^{atm} increased at 1.59 ppm yr^{-1}, while global-mean pCO_2^{sw} in both model configurations increased at slightly lower rates: 1.56 (CORE) and 1.52 ppm yr^{-1} (coupled). The model results are consistent with observations in this regard; regional discrepancies from the atmospheric trend are evident, but as a whole the surface ocean tracks the atmosphere. It is important to note that the coupled model's climate sensitivity over the twentieth century leads to surface ocean warming in excess of that observed; because of greater warming in the coupled simulation, relative to the CORE-forced run, a greater proportion of the trend in pCO_2^{sw} was due to temperature in the coupled model.

A key question is whether the CESM coupled model can accurately represent the impact of climate variability on carbon cycle dynamics. We presented an analysis of the mechanisms driving interannual variability in sea–air fluxes. The impact of climate variability on sea–air fluxes is similar between the model and observational estimates. Variability in the coupled model was weak, relative to that simulated by the CORE-forced model. The basic structure of the coupled model's response to key climate modes was similar to observational metrics and the CORE-forced integration; however, the response to variability in the coupled model differed in its regional detail.

Uptake and storage of C_{ant} in the Southern Ocean remains a problematic feature of coarse resolution global carbon cycle simulations. In particular, the ventilation and formation of intermediate and mode waters in the Southern Ocean is not well captured by the model. A related issue is the substantial Southern Ocean mixed layer biases, which are too shallow by 30–50 m in the ACC during summer and by 100–400 m during winter. Mixed layer depths interact with the processes controlling ventilation. For instance, in the model the boundary layer depth sets the near-surface region over which the eddy-mixing coefficient is the maximum. Substantial improvements in the physical parameterizations controlling mixing and overturning in the model are necessary to improve the representation of ventilation. The current CESM configuration can be expected to continue to underestimate C_{ant} uptake under twenty-first-century scenarios.

REFERENCES

Armstrong, R., C. Lee, J. Hedges, S. Honjo, and S. Wakeham, 2002: A new, mechanistic model for organic carbon fluxes in the ocean based on the quantitative association of POC with ballast minerals. *Deep-Sea Res. II,* **49,** 219–236, doi:10.1016/S0967-0645(01)00101-1.

Arrigo, K. R., G. van Dijken, and S. Bushinsky, 2008a: Primary production in the Southern Ocean, 1997–2006. *J. Geophys. Res.,* **113,** C08004, doi:10.1029/2007JC004551.

——, ——, and M. C. Long, 2008b: Coastal Southern Ocean: A strong anthropogenic CO_2 sink. *Geophys. Res. Lett.,* **35,** L21602, doi:10.1029/2008GL035624.

Cerovecki, I., L. Talley, and M. Mazloff, 2011: A comparison of Southern Ocean air–sea buoyancy flux from an ocean state estimate with five other products. *J. Climate,* **24,** 6283–6306.

Chavez, F. P., P. G. Strutton, G. E. Friederich, R. A. Feely, G. C. Feldman, D. G. Foley, and M. J. McPhaden, 1999: Biological and chemical response of the equatorial Pacific Ocean to the 1997–98 El Niño. *Science,* **286,** 2126–2131, doi:10.1126/science.286.5447.2126.

Crutzen, P., 2006: The "anthropocene." *Earth System Science in the Anthropocene,* E. Ehlers and T. Krafft, Eds., Springer Berlin Heidelberg, 13–18.

Danabasoglu, G., and J. Marshall, 2007: Effects of vertical variations of thickness diffusivity in an ocean general circulation model. *Ocean Modell.,* **18,** 122–141, doi:10.1016/j.ocemod.2007.03.006.

——, W. G. Large, and B. P. Briegleb, 2010: Climate impacts of parameterized Nordic sea overflows. *J. Geophys. Res.,* **115,** C11005, doi:10.1029/2010JC006243.

——, S. Bates, B. P. Briegleb, S. R. Jayne, M. Jochum, W. G. Large, S. Peacock, and S. G. Yeager, 2012: The CCSM4 ocean component. *J. Climate,* **25,** 1361–1389.

Dickson, A. G., and C. Goyet, Eds., 1994: Handbook of methods for the analysis of the various parameters of the carbon dioxide system in sea water: Version 2. Oak Ridge National Lab Tech. Rep. ORNL/CDIAC-74, 187 pp.

Doney, S. C., D. M. Glover, S. J. McCue, and M. Fuentes, 2003: Mesoscale variability of Sea-Viewing Wide Field-of-View Sensor (SeaWiFS) satellite ocean color: Global patterns

and spatial scales. *J. Geophys. Res.,* **108,** 3024, doi:10.1029/2001JC000843.

——, and Coauthors, 2004: Evaluating global ocean carbon models: The importance of realistic physics. *Global Biogeochem. Cycles,* **18,** GB3017, doi:10.1029/2003GB002150.

——, K. Lindsay, I. Fung, and J. John, 2006: Natural variability in a stable, 1000-yr global coupled climate–carbon cycle simulation. *J. Climate,* **19,** 3033–3054.

——, S. Yeager, G. Danabasoglu, W. G. Large, and J. C. McWilliams, 2007: Mechanisms governing interannual variability of upper-ocean temperature in a global ocean hindcast simulation. *J. Phys. Oceanogr.,* **37,** 1918–1938.

——, I. Lima, R. Feely, D. Glover, K. Lindsay, N. Mahowald, J. Moore, and R. Wanninkhof, 2009a: Mechanisms governing interannual variability in upper-ocean inorganic carbon system and air–sea CO_2 fluxes: Physical climate and atmospheric dust. *Deep-Sea Res. II,* **56,** 640–655, doi:10.1016/j.dsr2.2008.12.006.

——, and Coauthors, 2009b: Skill metrics for confronting global upper ocean ecosystem-biogeochemistry models against field and remote sensing data. *J. Mar. Syst.,* **76,** 95–112, doi:10.1016/j.jmarsys.2008.05.015.

Farneti, R., and P. R. Gent, 2011: The effects of the eddy-induced advection coefficient in a coarse-resolution coupled climate model. *Ocean Modell.,* **39,** 135–145, doi:10.1016/j.ocemod.2011.02.005.

Feely, R. A., R. Wanninkhof, T. Takahashi, and P. Tans, 1999: Influence of El Niño on the equatorial Pacific contribution to atmospheric CO_2 accumulation. *Nature,* **398,** 597–601, doi:10.1038/19273.

Fox-Kemper, B., and Coauthors, 2010: Parameterization of mixed layer eddies. III: Implementation and impact in global ocean climate simulations. *Ocean Modell.,* **39,** 61–78, doi:10.1016/j.ocemod.2010.09.002.

Friedlingstein, P., and Coauthors, 2006: Climate–carbon cycle feedback analysis: Results from the C⁴MIP model intercomparison. *J. Climate,* **19,** 3337–3353.

Fung, I. Y., S. C. Doney, K. Lindsay, and J. John, 2005: Evolution of carbon sinks in a changing climate. *Proc. Natl. Acad. Sci. USA,* **102,** 11 201–11 206, doi:10.1073/pnas.0504949102.

Garcia, H. E., R. A. Locarnini, T. P. Boyer, and J. I. Antonov, 2006: *Nutrients (phosphate, nitrate, silicate).* Vol. 4, *World Ocean Atlas 2005,* NOAA Atlas NESDIS 64, 396 pp.

Gent, P. R., 2011: The Gent–McWilliams parameterization: 20/20 hindsight. *Ocean Modell.,* **39,** 2–9, doi:10.1016/j.ocemod.2010.08.002.

——, and J. McWilliams, 1990: Isopycnal mixing in ocean circulation models. *J. Phys. Oceanogr.,* **20,** 150–155.

——, and G. Danabasoglu, 2011: Response to increasing Southern Hemisphere winds in CCSM4. *J. Climate,* **24,** 4992–4998.

——, and Coauthors, 2011: The Community Climate System Model version 4. *J. Climate,* **24,** 4973–4991.

Griffies, S., and Coauthors, 2009: Coordinated Ocean-Ice Reference Experiments (COREs). *Ocean Modell.,* **26,** 1–46, doi:10.1016/j.ocemod.2008.08.007.

Gruber, N., J. L. Sarmiento, and T. F. Stocker, 1996: An improved method for detecting anthropogenic CO_2 in the oceans. *Global Biogeochem. Cycles,* **10,** 809–837, doi:10.1029/96GB01608.

——, and Coauthors, 2009: Oceanic sources, sinks, and transport of atmospheric CO_2. *Global Biogeochem. Cycles,* **23,** GB1005, doi:10.1029/2008GB003349.

Hunke, E., and W. Lipscomb, 2008: CICE: The Los Alamos sea ice model documentation and software user's manual, version 4.0.

Los Alamos National Laboratory Tech. Rep. LA-CC-06-012, 76 pp.

Hurrell, J. W., 1995: Decadal trends in the North Atlantic Oscillation: Regional temperatures and precipitation. *Science,* **269,** 676–679, doi:10.1126/science.269.5224.676.

——, J. J. Hack, D. Shea, J. M. Caron, and J. Rosinski, 2008: A new sea surface temperature and sea ice boundary dataset for the community atmosphere model. *J. Climate,* **21,** 5145–5153.

Kalnay, E., and Coauthors, 1996: The NCEP/NCAR 40-Year Reanalysis Project. *Bull. Amer. Meteor. Soc.,* **77,** 437–471.

Key, R. M., and Coauthors, 2004: A global ocean carbon climatology: Results from Global Data Analysis Project (GLODAP). *Global Biogeochem. Cycles,* **18,** GB4031, doi:10.1029/2004GB002247.

Krishnamurthy, A., J. K. Moore, C. S. Zender, and C. Luo, 2007: Effects of atmospheric inorganic nitrogen deposition on ocean biogeochemistry. *J. Geophys. Res.,* **112,** G02019, doi:10.1029/2006JG000334.

——, ——, N. Mahowald, C. Luo, S. Doney, K. Lindsay, and C. S. Zender, 2009: Impacts of increasing anthropogenic soluble iron and nitrogen deposition on ocean biogeochemistry. *Global Biogeochem. Cycles,* **23,** GB3016, doi:10.1029/2008GB003440.

Lamarque, J.-F., and Coauthors, 2010: Historical (1850–2000) gridded anthropogenic and biomass burning emissions of reactive gases and aerosols: Methodology and application. *Atmos. Chem. Phys.,* **10,** 7017–7039, doi:10.5194/acp-10-7017-2010.

Landrum, L., M. M. Holland, D. P. Schneider, and E. Hunke, 2012: Antarctic sea ice climatology, variability, and late twentieth-century change in CCSM4. *J. Climate,* **25,** 4817–4838.

Large, W. G., and S. Yeager, 2009: The global climatology of an interannually varying air–sea flux data set. *Climate Dyn.,* **33,** 341–364, doi:10.1007/s00382-008-0441-3.

——, J. C. McWilliams, and S. C. Doney, 1994: Oceanic vertical mixing: A review and a model with a nonlocal boundary layer parameterization. *Rev. Geophys.,* **32,** 363–403, doi:10.1029/94RG01872.

Lawrence, D. M., K. W. Oleson, M. G. Flanner, C. G. Fletcher, P. J. Lawrence, S. Levis, S. C. Swenson, and G. B. Bonan, 2012: The CCSM4 land simulation, 1850–2005: Assessment of surface climate and new capabilities. *J. Climate,* **25,** 2240–2260.

Le Quéré, C., and Coauthors, 2009: Trends in the sources and sinks of carbon dioxide. *Nat. Geosci.,* **2,** 831–836, doi:10.1038/ngeo689.

——, T. Takahashi, E. T. Buitenhuis, C. Rödenbeck, and S. C. Sutherland, 2010: Impact of climate change and variability on the global oceanic sink of CO_2. *Global Biogeochem. Cycles,* **24,** GB4007, doi:10.1029/2009GB003599.

Lovenduski, N. S., N. Gruber, S. C. Doney, and I. D. Lima, 2007: Enhanced CO_2 outgassing in the Southern Ocean from a positive phase of the southern annular mode. *Global Biogeochem. Cycles,* **21,** GB2026, doi:10.1029/2006GB002900.

——, ——, and ——, 2008: Toward a mechanistic understanding of the decadal trends in the Southern Ocean carbon sink. *Global Biogeochem. Cycles,* **22,** GB3016, doi:10.1029/2007GB003139.

——, M. C. Long, P. R. Gent, and K. Lindsay, 2013: Multi-decadal trends in the advection and mixing of natural carbon in the Southern Ocean. *Geophys. Res. Lett.,* **40,** 139–142, doi:10.1029/2012GL054483.

Marshall, J., and T. Radko, 2003: Residual-mean solutions for the Antarctic Circumpolar Current and its associated overturning circulation. *J. Phys. Oceanogr.,* **33,** 2341–2354.

Matsumoto, K., and N. Gruber, 2005: How accurate is the estimation of anthropogenic carbon in the ocean? An evaluation of the ΔC^* method. *Global Biogeochem. Cycles,* **19,** GB3014, doi:10.1029/2004GB002397.

McKinley, G. A., A. R. Fay, T. Takahashi, and N. Metzl, 2011: Convergence of atmospheric and North Atlantic carbon dioxide trends on multidecadal timescales. *Nat. Geosci.,* **4,** 606–610, doi:10.1038/ngeo1193.

Metzl, N., 2009: Decadal increase of oceanic carbon dioxide in southern Indian Ocean surface waters (1991–2007). *Deep-Sea Res. II,* **56,** 607–619, doi:10.1016/j.dsr2.2008.12.007.

Mikaloff Fletcher, S. E., and Coauthors, 2006: Inverse estimates of anthropogenic CO_2 uptake, transport, and storage by the ocean. *Global Biogeochem. Cycles,* **20,** GB2002, doi:10.1029/2005GB002530.

——, and Coauthors, 2007: Inverse estimates of the oceanic sources and sinks of natural CO_2 and the implied oceanic carbon transport. *Global Biogeochem. Cycles,* **21,** GB1010, doi:10.1029/2006GB002751.

Moore, J. K., and M. R. Abbott, 2000: Phytoplankton chlorophyll distributions and primary production in the Southern Ocean. *J. Geophys. Res.,* **105** (C12), 28 709–28 722.

——, S. C. Doney, J. A. Kleypas, D. M. Glover, and I. Y. Fung, 2002: An intermediate complexity marine ecosystem model for the global domain. *Deep-Sea Res. II,* **49,** 403–462, doi:10.1016/S0967-0645(01)00108-4.

——, ——, and K. Lindsay, 2004: Upper ocean ecosystem dynamics and iron cycling in a global three-dimensional model. *Global Biogeochem. Cycles,* **18,** GB4028, doi:10.1029/2004GB002220.

——, K. Lindsay, S. C. Doney, M. C. Long, and K. Misumi, 2013: Marine ecosystem dynamics and biogeochemical cycling in the Community Earth System Model [CESM1(BGC)]: Comparison of the 1990s with the 2090s under the RCP 4.5 and RCP 8.5 scenarios. *J. Climate,* in press.

Najjar, R., and J. Orr, 1998: Design of OCMIP-2 simulations of chlorofluorocarbons, the solubility pump and common biogeochemistry. IPSL, 19 pp. [Available online at http://ocmip5.ipsl.jussieu.fr/OCMIP/phase2/simulations/design.ps.]

Nakamura, T., T. Toyoda, Y. Ishikawa, and T. Awaji, 2006: Effects of tidal mixing at the Kuril Straits on North Pacific ventilation: Adjustment of the intermediate layer revealed from numerical experiments. *J. Geophys. Res.,* **111,** C04003, doi:10.1029/2005JC003142.

Neale, R. B., J. Richter, S. Park, P. H. Lauritzen, S. J. Vavrus, P. J. Rasch, and M. Zhang, 2013: The mean climate of the Community Atmosphere Model version 4 (CAM4) in forced SST and coupled experiments. *J. Climate,* **26,** 5150–5168.

Park, G., and Coauthors, 2010: Variability of global net sea–air CO_2 fluxes over the last three decades using empirical relationships. *Tellus,* **62B,** 352–368, doi:10.1111/j.1600-0889.2010.00498.x.

Russell, J., R. Stouffer, and K. Dixon, 2006: Intercomparison of the Southern Ocean circulations in IPCC coupled model control simulations. *J. Climate,* **19,** 4560–4575.

Sabine, C. L., and Coauthors, 2004: The oceanic sink for anthropogenic CO_2. *Science,* **305,** 367–371, doi:10.1126/science.1097403.

Sarmiento, J., and N. Gruber, 2006: *Ocean Biogeochemical Dynamics.* Princeton University Press, 526 pp.

Smith, R. D., and Coauthors, 2010: The Parallel Ocean Program (POP) reference manual. Los Alamos National Laboratory Tech. Rep. LAUR-10-01853, 140 pp.

Takahashi, T., R. Feely, R. Weiss, R. Wanninkhof, D. Chipman, S. Sutherland, and T. Takahashi, 1997: Global air–sea flux of CO_2: An estimate based on measurements of sea–air pCO_2 difference. *Proc. Natl. Acad. Sci. USA,* **94,** 8292–8299.

——, and Coauthors, 2002: Global sea–air CO_2 flux based on climatological surface ocean pCO_2, and seasonal biological and temperature effects. *Deep-Sea Res. II,* **49,** 1601–1622, doi:10.1016/S0967-0645(02)00003-6.

——, and Coauthors, 2009: Climatological mean and decadal change in surface ocean pCO_2, and net sea–air CO_2 flux over the global oceans. *Deep-Sea Res. II,* **56,** 554–577, doi:10.1016/j.dsr2.2008.12.009.

Thomas, H., A. E. Friederike Prowe, I. D. Lima, S. C. Doney, R. Wanninkhof, R. J. Greatbatch, U. Schuster, and A. Corbière, 2008: Changes in the North Atlantic Oscillation influence CO_2 uptake in the North Atlantic over the past 2 decades. *Global Biogeochem. Cycles,* **22,** GB4027, doi:10.1029/2007GB003167.

Thompson, D. W. J., and S. Solomon, 2002: Interpretation of recent Southern Hemisphere climate change. *Science,* **296,** 895–899, doi:10.1126/science.1069270.

Thornton, P., and Coauthors, 2009: Carbon-nitrogen interactions regulate climate-carbon cycle feedbacks: Results from an atmosphere-ocean general circulation model. *Biogeosciences,* **6,** 2099–2120, doi:10.5194/bg-6-2099-2009.

Toggweiler, J. R., and J. Russell, 2008: Ocean circulation in a warming climate. *Nature,* **451,** 286–288, doi:10.1038/nature06590.

Trenberth, K. E., 1997: The definition of El Niño. *Bull. Amer. Meteor. Soc.,* **78,** 2771–2777.

Wang, G., and D. Schimel, 2003: Climate change, climate modes, and climate impacts. *Annu. Rev. Environ. Resour.,* **28,** 1–28, doi:10.1146/annurev.energy.28.050302.105444.

Wang, S., and J. K. Moore, 2012: Variability of primary production and air-sea CO_2 flux in the Southern Ocean. *Global Biogeochem. Cycles,* **26,** GB1008, doi:10.1029/2010GB003981.

——, F. W. Primeau, and S. Khatiwala, 2012: Simulation of anthropogenic CO_2 uptake in the CCSM3.1 ocean circulation-biogeochemical model: Comparison with data-based estimates. *Biogeosciences,* **9,** 1321–1336, doi:10.5194/bg-9-1321-2012.

Wanninkhof, R., 1992: Relationship between wind speed and gas exchange over the ocean. *J. Geophys. Res.,* **97** (C5), 7373–7382.

Weijer, W., and Coauthors, 2012: The Southern Ocean and its climate in CCSM4. *J. Climate,* **25,** 2652–2675.

Weiss, R. F., 1974: Carbon dioxide in seawater: The solubility of an ideal gas. *Mar. Chem.,* **2,** 203–215, doi:10.1016/0304-4203(74)90015-2.

——, and B. Price, 1980: Nitrous oxide solubility in water and seawater. *Mar. Chem.,* **8,** 347–359, doi:10.1016/0304-4203(80)90024-9.

Zwiers, F. W., and H. von Storch, 1995: Taking serial correlation into account in tests of the mean. *J. Climate,* **8,** 336–351.